

# An Updated Investigation of Post-Transformation Intensity, Structural, and Duration Extremes for Extratropically Transitioning North Atlantic Tropical Cyclones

GIORGIO SARRO<sup>a,b</sup> AND CLARK EVANS<sup>a</sup>

<sup>a</sup> Atmospheric Science Program, University of Wisconsin–Milwaukee, Milwaukee, Wisconsin

<sup>b</sup> Department of Geophysical Sciences, University of Chicago, Chicago, Illinois

(Manuscript received 25 March 2022, in final form 29 June 2022)

**ABSTRACT:** The transformation stage of extratropical transition characterizes the process by which a tropical cyclone transforms into an extratropical cyclone at higher latitudes in a cooler, more baroclinic environment. A 2006 study connects extremes in transformation-stage duration, post-transformation intensity change, and post-transformation thermal structure for North Atlantic basin tropical cyclones to synoptic-scale environmental variability. However, the 2006 study's findings are derived from coarse atmospheric analyses that include fictitious tropical cyclone vortices applied to small samples with substantial variability between cases. This study updates the 2006 study's findings using larger sample sizes, improvements in atmospheric reanalysis resolution and fidelity, and advances in scientific understanding over the last two decades. Transformation-stage duration is primarily a function of the duration that a transforming cyclone remains in an environment supportive of tropical development after entering a region supportive of baroclinic development. Post-transformation intensity-change composites are distinguished primarily by whether proper phasing is achieved between the transforming cyclone and upstream trough following the transformation stage. Finally, post-transformation thermal structure is distinguished primarily by whether the transforming cyclone moves into a strongly confluent synoptic-scale environment following the transformation stage. This study also presents the first composite analyses of North Atlantic tropical cyclones that maintain a lower-tropospheric warm-core structure post-transformation, termed instant warm-seclusion cyclones, which have previously only been diagnosed in case studies of individual North Atlantic tropical cyclones and for a limited climatology of western North Pacific tropical cyclones. These cyclones, comprising approximately one-third of all cases, are characterized by the transforming TC becoming negatively tilted with respect to the upstream trough and undergoing cyclonic Rossby wave breaking.

**KEYWORDS:** Extratropical cyclones; Extratropical transition; Tropical cyclones

## 1. Introduction

Extratropical transition (ET) is the process by which a tropical cyclone (TC), upon encountering a baroclinic environment and reduced sea surface temperature (SST) at higher latitudes, transforms into an extratropical cyclone (Jones et al. 2003; Evans et al. 2017). The transformation of a TC into an extratropical cyclone during ET is characterized by the acquisition of frontal structures as the TC interacts with the midlatitude baroclinic zone (e.g., Klein et al. 2000; Kitabatake 2008) and, in many cases, the loss of the TC's warm-core structure in favor of a cold-core structure typical of midlatitude extratropical cyclones (e.g., Evans and Hart 2003; Hart 2003; Hart et al. 2006, hereafter H06). The resultant extratropical cyclone following ET can bring intense precipitation, very large waves, and even hurricane-force winds to populated regions and shipping corridors at higher latitudes where tropical-like impacts are less common (Jones et al. 2003). Furthermore, the large-scale flow reconfiguration that can be fostered by the interaction of a recurving TC with the midlatitude flow during ET can result in downstream high-impact weather events well-removed from the TC itself (Jones et al. 2003; Keller et al. 2019).

The cyclone phase space (CPS; Evans and Hart 2003; Hart 2003) has become widely accepted in the research and operational communities to objectively characterize the frontal

and thermal-structure evolutions that accompany ET (Evans et al. 2017). The CPS describes a cyclone's structure via three parameters: 900–600-hPa thermal wind ( $-V_T^L$ ), 600–300-hPa thermal wind ( $-V_T^U$ ), and 900–600-hPa cyclone-motion-relative thickness asymmetry ( $B$ ), all measured within a 500-km radius of the cyclone's center. Positive values of  $-V_T^L$  or  $-V_T^U$  represent a warm-core structure in their respective layers, whereas large positive values of  $B$  indicate a frontal cyclone with a thermally direct circulation. The start of ET's transformation stage (as first defined by Klein et al. 2000) is characterized by  $B$  exceeding 10 m and its end is characterized by  $-V_T^L$  becoming negative (Evans and Hart 2003), though some TCs lose their lower-tropospheric warm-core structure before acquiring frontal structures (Wood and Ritchie 2014; Studholme et al. 2015; Bieli et al. 2019b).

Following the transformation stage, the now-extratropical cyclone can slowly dissipate or reintensify as an extratropical cyclone (Klein et al. 2000; H06). The now-extratropical cyclone can also maintain a cold-core or develop a warm-seclusion (Shapiro and Keyser 1990) thermal structure. The only composite evaluation to-date of post-transformation cyclone outcomes such as these is H06. In their study, cyclones that reintensify post-transformation do so when the approaching upstream trough facilitating ET is negatively tilted, which is argued to enhance an eddy cyclonic potential vorticity (PV) flux (following Molinari et al. 1995) toward the cyclone, but decay when the approaching upstream trough is positively tilted.

Corresponding author: Clark Evans, evans36@uwm.edu

DOI: 10.1175/MWR-D-22-0088.1

© 2022 American Meteorological Society. For information regarding reuse of this content and general copyright information, consult the AMS Copyright Policy ([www.ametsoc.org/PUBSReuseLicenses](http://www.ametsoc.org/PUBSReuseLicenses)).

Unauthenticated | Downloaded 01/16/23 08:41 PM UTC

Further, H06 indicate that post-transformation extratropical cyclones develop a warm-seclusion structure when the upstream trough facilitating ET is of comparable horizontal and vertical extent to that of the transforming cyclone. Finally, H06's accompanying evaluation of transformation-stage duration indicates that rapidly transforming TCs (those that complete transformation in an anomalously short time) are associated with a higher-amplitude upstream trough than are slowly transforming TCs (those that complete transformation in an anomalously long time) because the higher-amplitude upstream trough advects the TC more-rapidly poleward across the underlying SST gradient and midlatitude baroclinic zone.

Although the H06 results are believed to be scientifically sound, their findings merit an updated investigation for several reasons. First, the synoptic environments of several post-transformation intensifying TCs studied by H06 or later investigators (Thornicroft and Jones 2000; Evans and Prater-Mayes 2004; Sun et al. 2012) do not comport with H06's composite analysis. This is likely reflective of the small number of TCs comprising this (6–11) and each of H06's composites. Further, H06's composite analyses are generated using a coarse atmospheric analysis dataset ( $1^{\circ}$  horizontal grid spacing from the U.S. Navy's NOGAPS model; Hogan and Rosmond 1991) that includes a bogussed (or artificially prescribed) TC vortex (Goerss and Jeffries 1994), which Jones et al. (2003) hypothesized can impact the model analyses' representation of ET. Consequently, this study's primary goal is to update H06's analysis using state-of-the-art high-resolution atmospheric reanalysis data applied to larger, presumably more representative samples. The resulting analysis supports H06's transformation-stage duration results, provides expanded insights into H06's post-transformation intensity-change results, and provides new insights into the large-scale environments supporting post-transformation warm-seclusion structural development. Furthermore, this study introduces a hitherto understudied ET classification in which TCs develop a warm-seclusion structure directly from the tropical phase without first acquiring a cold-core structure, here termed instant warm-seclusion.

The remainder of this paper is structured as follows. Section 2 describes the data and methodology used to partition candidate TCs into their respective duration, intensity-change, and thermal-structure composites. Section 3 analyzes the factors that facilitate a TC rapidly versus slowly transforming into an extratropical cyclone, intensify or weaken post-transformation, and develop a warm-seclusion structure versus maintain a cold-core structure post-transformation. Section 4 discusses instant warm-seclusion events and analyzes the environmental conditions associated with their development. Section 5 closes the paper with a summary of the study's key findings and discussion of some of the results' implications.

## 2. Methodology

### a. Data

Candidate TCs are selected from National Hurricane Center (NHC) best track data (Landsea and Franklin 2013) between 1995 and 2019. This 25-yr period is over 4 times longer than the

6-yr period (1998–2003) considered by H06, and the resulting 167 ET events is also 4 times larger than the 42 ET events considered by H06.

The ERA5 reanalysis (Hersbach et al. 2020) at 6-hourly temporal frequency (to match NHC TC advisory frequency) and  $0.25^{\circ}$  horizontal grid spacing is used to diagnose TC CPS pathways and generate composites of selected atmospheric fields. Full details of the atmospheric modeling system, observations, and assimilation methods used in ERA5 are provided by Hersbach et al. (2020). ERA5's improved resolution relative to the previous-generation ERA-Interim (Dee et al. 2011) reanalysis enables ERA5 to depict TC structure (Dullaart et al. 2019; Hersbach 2019; Malakar et al. 2020; Bian et al. 2021) and intensity (Malakar et al. 2020; Bian et al. 2021) more reliably than ERA-Interim. Nevertheless, ERA5 systematically underestimates TC intensity (Sainsbury et al. 2020; Malakar et al. 2020) and outer size (Bian et al. 2021) as compared to best track estimates and satellite observations, respectively, particularly for the most-intense TCs [e.g., those with maximum sustained 10-m wind speeds greater than  $\sim 90$  kt ( $\sim 46 \text{ m s}^{-1}$ ); Malakar et al. 2020]. The ERA5 depictions of the ET events considered in this study are realistic for all but the weakest and smallest TCs (not shown), for which a localized sea level pressure minimum (as defined by the presence of a closed isobar at a 2-hPa interval) cannot always be reliably detected.

Because SST data available in ERA5 are drawn from different data sources before versus after August 2007 (Hersbach et al. 2020, their Table 7), SST data used to compute TC potential intensities (as described in section 2g) are instead drawn from the NOAA Optimum Interpolation SST V2 (Reynolds et al. 2007) dataset at  $0.25^{\circ}$  horizontal grid spacing.

### b. Normalizing the ET timeline

All candidate TC paths through the CPS are computed using ERA5 reanalysis data for an 8-day period extending 5 days prior through 3 days after the best track time at which each TC is first classified as extratropical. A 24-h running smoother is applied to all CPS output following Hart (2003) and H06. A CPS-based normalized ET timeline (Evans and Hart 2003; H06) is then established to diagnose ET occurrence and the timing of selected ET milestones, allowing for ET-related processes to be isolated across a common timeline for all TCs. Specifically, the beginning of ET ( $T_B$ ) marks the time when the cyclone becomes significantly asymmetric ( $B > 10$ ), and the end of ET ( $T_E$ ) marks the time when the lower-tropospheric thermal wind indicates a cold-core cyclone ( $-V_T^L < 0$ ). Following H06, three additional milestones,  $T_B - 24$  h,  $T_{\text{MID}} [= (1/2)(T_B + T_E)]$ , and  $T_E + 24$  h, are defined to aid in examining how the synoptic-scale environments within which TCs undergo ET evolve leading into, during, and following the completion of the transformation stage. All five times correspond to the closest 6-hourly synoptic time (0000, 0600, 1200, or 1800 UTC) at or after the milestone is reached.

### c. Case selection

The NHC tracked 376 North Atlantic TCs between 1995 and 2019, of which 167 (44.4%) are operationally classified as transforming from a purely tropical to a purely extratropical

TABLE 1. Summary of the outcomes of the TC screening process used in this study.

Initial candidate TCs	167
Dissipation within 24 h of $T_E$	63
No identifiable $T_B$	2
Poorly resolved by ERA5 and CPS	20
Dissipation as warm-core remnant low	4
Retained extratropically transforming TCs	78
TCs following the Evans and Hart (2003) ET pathway	52
TCs that complete the transformation stage without first acquiring a cold-core thermal structure	26

cyclone. This percentage is consistent with previous North Atlantic ET climatologies (Hart and Evans 2001; Bieli et al. 2019a,b).

Prior to generating composites, these 167 candidate TCs are screened to ensure the following characteristics:

- Persistence as a distinct cyclone (i.e., not having a best track classification of dissipating or merging with another cyclone) for at least 24 h following the best track–determined  $T_E$ . This is necessary to diagnose post-transformation intensity-change and thermal-structure outcomes. This criterion eliminates 63 TCs from consideration. Although H06 did not eliminate these TCs from their transformation-stage duration analysis, we do so to ensure consistent samples for the bootstrap significance analysis introduced in section 2f.
- An identifiable CPS-derived  $T_B$ . Two candidate TCs formed with  $B > 10$  m, indicating substantial lower-tropospheric across-track thermal asymmetry at their genesis. As a result,  $T_B$  cannot be identified and thus a full cyclone trajectory through the CPS cannot be obtained for these cases.
- Realistic CPS-derived structural evolution during ET. Though ERA5 can resolve TC and extratropical cyclone inner-core structure with greater fidelity relative to ERA-Interim and NOGAPS from prior studies, it is still limited in its ability to realistically depict thermal structure evolution for some TCs. This renders CPS diagnostics unreliable for these cases, eliminating a further 20 TCs [most of which have best track lifetime-maximum 10-m wind speeds of  $<50$  kt ( $25.77 \text{ m s}^{-1}$ )] from consideration. Representative TCs include Franklin (2011; asymmetric cold-core to symmetric cold-core structural transformation during ET), Bonnie (2016; CPS parameters near their ET-threshold values, as described in Evans and Hart 2003, at all analysis times), and Julia (2016; asymmetric warm-core to symmetric warm-core structural transformation during ET).
- Acquisition of extratropical cyclone structure (e.g., distinct frontal boundaries and asymmetric precipitation and wind-field distributions; Klein et al. 2000) in satellite and ERA5 reanalysis data. Four TCs classified as having completed ET in the NHC best track data do not have an ERA5-assessed  $T_E$ , nor do satellite data or ERA5-derived synoptic analyses indicate that these TCs acquire the structural hallmarks of extratropical cyclones. Consequently, these candidate TCs are considered herein to instead be post-tropical remnant lows.

The remaining 78 TCs are listed in Table 1. There is good agreement between the NHC best track–determined and

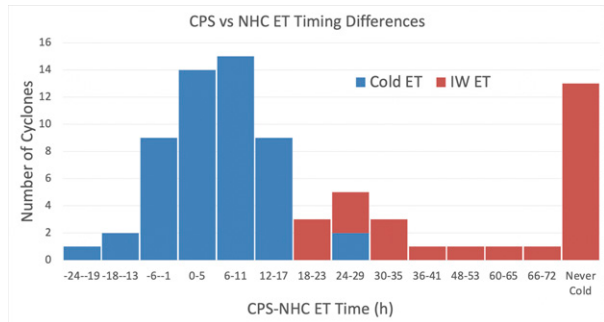


FIG. 1. Timing difference (h) between the NHC best track–determined and ERA5-based CPS-determined  $T_E$ , defined as  $T_{E,\text{CPS}} - T_{E,\text{NHC}}$ , for (blue) all post-transformation cold-core TCs and (red) all post-transformation instant warm-seclusion TCs. The last bar, labeled “Never Cold,” indicates the post-transformation instant warm-seclusion TCs that dissipate as an extratropical cyclone without ever transforming into a cold-core extratropical cyclone. No TCs have timing discrepancies of 42–47 or 54–59 h, such that these bins are not displayed.

ERA5-derived  $T_E$  for most of these TCs (Fig. 1), with 38 (48.7%) having an ERA5-derived  $T_E$  within  $\pm 6$  h of the best track–determined  $T_E$ . This is consistent with Evans and Hart (2003), wherein 20/38 (52.6%) of TCs have a CPS-derived  $T_E$  within  $\pm 6$  h of the best track–determined  $T_E$ , but not with Bieli et al. (2019b), wherein the ERA-Interim-derived  $T_E$  occurs an average of 32 h earlier than the best track–determined  $T_E$ . The latter’s inconsistency may be the result of a propensity for low values of the CPS  $-V_T^L$  and  $-V_T^U$  thermal-wind parameters in the ERA-Interim reanalysis (Bieli et al. 2019a) that is not apparent in the ERA-15 and ERA5 reanalysis data used in Evans and Hart (2003) and the present study.

Despite the overall agreement between the NHC best track–determined and ERA-derived  $T_E$  for most of the 78 TCs, however, the ERA5-derived  $T_E$  is at least 18 h later than the best track–derived  $T_E$  for 28 TCs (Fig. 1). A timing discrepancy of +18 h is more than one standard deviation larger than the mean timing discrepancy for the 38 North Atlantic ET events considered by Evans and Hart (2003) and more than 2 days larger than the mean timing discrepancy for the 1979–2017 North Atlantic ET climatology of Bieli et al. (2019a,b), and thus these 28 TCs are manually analyzed to diagnose why the large timing discrepancies occur. Of these 28 TCs, 26 are subjectively deemed to acquire the frontal structures characteristic to extratropical cyclones (as inferred from satellite data, including the development of extensive stratiform clouds poleward and open-cell cumulus clouds equatorward and westward of the transforming TC, and ERA5-derived lower-tropospheric frontogenesis calculations, both following Klein et al. (2000)’s conceptual model of ET’s transformation stage) near the best track–derived  $T_E$ . This suggests that these TCs maintain persistent warm-core structure post-transformation. These TCs structurally resemble “seclusion–occlusion” ET events (Kitabatake 2008), wherein a TC acquires an extratropical warm-seclusion structure immediately upon transforming into an extratropical cyclone. These 26 TCs are

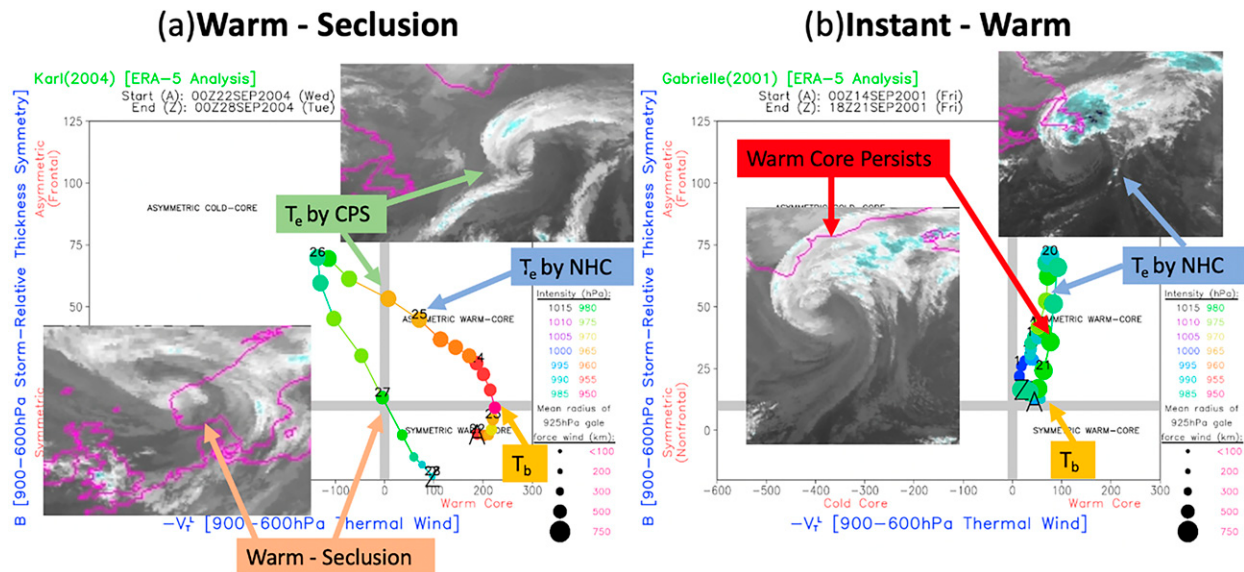


FIG. 2. Representative ERA5-based CPS examples (x axis:  $-V_T^L$ , y axis:  $B$ ; circle colors depict minimum sea level pressure and circle sizes depict the radius of 925-hPa gale-force winds, each per the legend at right in each panel; insets depict infrared satellite imagery at selected milestones obtained from the NOAA Global ISCCP B1 Browse System) of warm-seclusion cyclones. (a) A classical post-transformation warm-seclusion cyclone, here given by TC Karl (2004) and (b) an instant warm-seclusion event, here given by TC Gabrielle (2001).

hereafter termed *instant* warm seclusions to contrast them from the *post-transformation* warm seclusions of H06, which require that the TC first acquire an extratropical cold-core structure before acquiring a warm-seclusion thermal structure. Representative examples of post-transformation and instant warm seclusions are provided by TCs Karl (2004; Fig. 2a) and Gabrielle (2001, classified by H06 as having “extended hybrid existence” with a CPS-derived  $T_E$  90 h later than the best track-determined  $T_E$ ; Fig. 2b), respectively. Other North Atlantic examples in the refereed literature include TCs Lili (1996; Browning et al. 1998; Agustí-Panareda et al. 2005), Helene (2006; Pantillon et al. 2013), Igor (2010; Masson 2014), and Ophelia (2017; Rantanen et al. 2020).

It is possible that the prevalence of instant warm-seclusion events is an artifact of the ERA5 reanalysis rather than a plausible physical ET pathway. For instance, instant warm-seclusion TCs are more prevalent in the last 15 years of the climatology, corresponding to a marked increase in satellite data assimilated into ERA5 (Hersbach et al. 2020, their Figs. 3 and 5). However, we interpret this to suggest that ERA5 analyses for recent years can better resolve inner-core cyclone structures as compared to earlier years and prior reanalyses. In addition, the persistent warm-core structure exhibited by the 26 instant warm-seclusion TCs is not a function of the fine horizontal grid spacing of the ERA reanalysis, since coarsening these data from  $0.25^\circ$  to  $1^\circ$  horizontal grid spacing to match that of the NOGAPS analyses used by H06 does not alter the resulting CPS trajectories (not shown). Consequently, instant warm seclusions appear to represent a heretofore underappreciated structural outcome of ET—here representing 33% of ET events, in close agreement with the 35% of ET events over the 2-yr western North Pacific sample considered by Kitabatake (2008)—rather than an artifact of the present study’s methodology.

Consequently, there are two sets of TCs that undergo ET, totaling 78 TCs, considered in the remainder of this study:

- A set of 52 TCs (Table 2) that meet the above screening criteria and (for all but two TCs) have a CPS-determined  $T_E$  less than 18 h following the best track-determined  $T_E$ . This is 18 more TCs than are considered in H06’s transformation duration evaluation and 31 more TCs than are considered in H06’s post-transformation intensity-change and thermal-structure evaluations.
- A set of 26 instant warm seclusions (Table 3; Fig. 3d) that meet the screening criteria listed above and have a CPS-determined  $T_E$  18 h or more following the best track-determined  $T_E$ . Because the best track-determined  $T_E$  is believed to be more representative of the end of the transformation stage for these TCs, the best track-determined  $T_E$  is used for normalizing the ET timeline for these cases. As a result, this set of cases is considered separately to maintain consistency in the analysis.

#### d. Composite membership

As in H06, the 52 retained non-instant warm-seclusion TCs are classified separately by transformation-stage duration, post-transformation intensity change, and post-transformation thermal structure. For the transformation-stage duration and post-transformation intensity-change classifications,  $a \pm 0.5$  standard deviation (from the composite mean) threshold is used to separate events into their respective composites. This subjective threshold is chosen to ensure a sufficiently large sample of events are contained in each composite; fortuitously, it also results in nearly equal sample sizes between the extremes within these classifications.

Candidate TCs are separated into fast, slow, and average transformation-stage duration composites, with duration defined

TABLE 2. The 52 retained TCs and their respective composite categories. The TCs are sorted first by transformation-stage duration, then by post-transformation intensity change.

Name	Duration	Intensity change	Thermal structure 72-h post- $T_E$
Sandy 2012	Slow (102 h)	Weakening (33 hPa)	Cold
Harvey 2017	Slow (102 h)	Neutral (7 hPa)	Cold
Joaquin 2015	Slow (96 h)	Neutral (7 hPa)	Cold
Tomas 2010	Slow (66 h)	Neutral (1 hPa)	Cold
Gabrielle 2019	Slow (60 h)	Neutral (3 hPa)	Cold
Danielle 1998	Slow (60 h)	Neutral (0 hPa)	Warm
Nate 2005	Slow (54 h)	Neutral (3 hPa)	Cold
Arthur 2002	Slow (54 h)	Neutral (1 hPa)	Cold
Earl 2010	Slow (48 h)	Weakening (23 hPa)	Cold
Karl 2004	Slow (48 h)	Weakening (16 hPa)	Warm
Floyd 1999	Slow (48 h)	Neutral (7 hPa)	Cold
Arthur 2014	Slow (48 h)	Neutral (7 hPa)	Cold
Earl 1998	Slow (48 h)	Neutral (6 hPa)	Warm
Ernesto 2006	Slow (48 h)	Neutral (5 hPa)	Cold
Mitch 1998	Slow (48 h)	Strengthening (-3 hPa)	Warm
Gaston 2004	Slow (48 h)	Strengthening (-3 hPa)	Cold
Opal 1995	Average (42 h)	Weakening (16 hPa)	Cold
Katia 2011	Average (42 h)	Weakening (11 hPa)	Cold
Edouard 1996	Average (42 h)	Neutral (2 hPa)	Warm
Sebastien 2019	Average (42 h)	Neutral (0 hPa)	Warm
Gustav 2002	Average (36 h)	Neutral (7 hPa)	Cold
Allison 2001	Average (36 h)	Neutral (6 hPa)	Cold
Gordon 2006	Average (36 h)	Neutral (6 hPa)	Cold
Frances 2004	Average (36 h)	Neutral (4 hPa)	Cold
Fabian 2003	Average (36 h)	Neutral (2 hPa)	Cold
Ophelia 2005	Average (36 h)	Neutral (0 hPa)	Cold
Cristobal 2014	Average (36 h)	Strengthening (-3 hPa)	Cold
Irene 2011	Average (30 h)	Weakening (12 hPa)	Cold
Bertha 2014	Average (30 h)	Neutral (5 hPa)	Cold
Kate 2003	Average (30 h)	Strengthening (-6 hPa)	Warm
Erin 2001	Average (30 h)	Strengthening (-9 hPa)	Cold
Chantal 2007	Average (30 h)	Strengthening (-17 hPa)	Warm
Iris 1995	Average (30 h)	Strengthening (-27 hPa)	Warm
Delta 2005	Fast (24 h)	Weakening (17 hPa)	Cold
Maria 2017	Fast (24 h)	Weakening (16 hPa)	Cold
Gert 2017	Fast (24 h)	Weakening (10 hPa)	Cold
Andrea 2013	Fast (24 h)	Neutral (6 hPa)	Cold
Felix 1995	Fast (24 h)	Neutral (3 hPa)	Cold
Ophelia 2011	Fast (24 h)	Neutral (2 hPa)	Cold
Bill 2009	Fast (24 h)	Neutral (0 hPa)	Cold
Chris 2018	Fast (24 h)	Strengthening (-1 hPa)	Cold
Alex 2016	Fast (24 h)	Strengthening (-6 hPa)	Cold
Chantal 1995	Fast (18 h)	Neutral (4 hPa)	Cold
Gordon 2000	Fast (18 h)	Neutral (4 hPa)	Cold
Bertha 1996	Fast (18 h)	Neutral (1 hPa)	Cold
Alberto 2000	Fast (18 h)	Strengthening (-2 hPa)	Cold
Karl 1998	Fast (12 h)	Weakening (32 hPa)	Cold
Danielle 2010	Fast (12 h)	Neutral (6 hPa)	Cold
Gustav 2008	Fast (12 h)	Neutral (4 hPa)	Cold
Cindy 2005	Fast (12 h)	Neutral (0 hPa)	Cold
Ike 2008	Fast (12 h)	Strengthening (-1 hPa)	Cold
Nate 2017	Fast (6 h)	Neutral (7 hPa)	Cold

as  $T_E - T_B$ . The average transformation-stage duration for the full 52-case sample is 37.2 h, which is slightly longer than the 30-h average from the [Evans and Hart \(2003\)](#) climatology. For a one-half standard deviation value of 10.6 h, 16 TCs are classified as slow transformations ( $T_E - T_B > 47.5$  h; magenta

tracks in [Fig. 3a](#)) and 19 TCs are classified as fast transformations ( $T_E - T_B < 26.1$  h; blue tracks in [Fig. 3a](#)). This classification procedure differs from that of [H06](#), which used an arbitrary 18-h difference from the [Evans and Hart \(2003\)](#) 30-h average transformation-stage duration to define slow transformations as

TABLE 3. The 26 instant warm-seclusion cyclones. Since  $T_E$  for these cases is obtained from NHC best track rather than ERA5-based CPS data, these TCs are not part of the transformation-stage duration or post-transformation intensity-change composites for the 52 TCs in Table 2. The TCs are sorted first by transformation-stage duration, then by post-transformation intensity change.

Name	Duration (h)	Intensity change (hPa)
Gabrielle 2001	126	10
Helene 2018	60	-1
Luis 1995	60	-5
Tanya 1995	48	7
Ophelia 2017	42	19
Helene 2006	42	8
Igor 2010	42	5
Chris 2012	42	5
Isaac 2000	42	-14
Maria 2005	36	-6
Lili 1996	36	-7
Florence 2006	36	-13
Otto 2010	30	7
Rafael 2012	30	1
Allison 1995	30	-4
Barry 2007	30	-5
Hermine 2016	24	3
Harvey 2005	24	-3
Noel 2007	24	-12
Michael 2018	24	-13
Lorenzo 2019	18	4
Oscar 2018	18	-7
Nicole 2016	12	3
Erika 1997	6	8
Kate 2015	6	5
Alberto 2006	6	-24

those in which  $T_E - T_B \geq 48$  h and fast transformations as those in which  $T_E - T_B \leq 12$  h. Applying the H06 definitions to the 52-case sample in Table 2 results in only 6 fast transformations while not changing the number of slow transformations. However, this does not qualitatively impact the composite findings (not shown), and the resulting composites agree with their H06 counterparts (cf. section 3a to H06's section 4a).

Candidate TCs are also separated into post-transformation strengthening, weakening, and neutral intensity-change composites, defined following H06 by their change in best track minimum sea level pressure (MSLP) between  $T_E + 24$  h and  $T_E$ . The full-composite-mean MSLP change between these times is a weakening of 4.3 hPa, with one-half standard deviation about this mean equal to 4.9 hPa. These thresholds result in 11 strengthening ( $\text{MSLP}_{T_E+24\text{h}} - \text{MSLP}_{T_E} < -0.6$  hPa; magenta tracks in Fig. 3b) and 10 weakening ( $\text{MSLP}_{T_E+24\text{h}} - \text{MSLP}_{T_E} > 9.2$  hPa; blue tracks in Fig. 3b) TCs. The strengthening and weakening composite sizes are five more and one less than their respective H06 counterparts. As with transformation-stage duration, this classification procedure differs from that of H06, which excluded TCs over land and used a  $\pm 4$ -hPa MSLP difference from a no-change baseline to identify strengthening and weakening events. Applying the H06 definitions to the 52-case sample in Table 2 reduces the number of strengthening

TCs from 11 to 5 while increasing the number of weakening TCs from 10 to 27. As with transformation duration, this does not qualitatively impact the composite findings (not shown), and the resulting composites largely agree with their H06 counterparts (cf. section 3b to H06's section 4b).

Last, the 52 candidate TCs are classified based on their post-transformation thermal structure, namely, whether they retain a cold-core structure through  $T_E + 72$  h or reacquire a lower-tropospheric warm-core structure ( $-V_T^L > 0$ ; a representative example is given by 2004's TC Karl in Fig. 2a) at any time post-transformation. This classification procedure is identical to that of H06. Altogether, 9 TCs transform into warm-seclusion extratropical cyclones (magenta tracks in Fig. 3c) and 43 TCs retain a cold-core structure (light blue tracks in Fig. 3c) following transformation.

Most of the H06 classifications for the 1998–2003 TCs considered herein are retained despite different ET-duration and post-transformation intensity-change classification criteria and the use of ERA5 rather than NOGAPS data. That said, the resulting sample sizes are still small because of the filtering process outlined in section 2c. However, it is believed that this filtering process, coupled with the more-objective transformation duration and post-transformation intensity-change classification criteria, finer-resolution and higher-quality atmospheric reanalysis data, and more-flexible bootstrapping technique for evaluating statistical significance (section 2f) used in this study result in higher confidence in the composite analyses relative to H06.

#### e. Compositing

Following H06, a storm-centered 0.25° resolution grid spanning 30° latitude and 30° longitude is centered at the location of each cyclone at each of the five ET milestones for the three classifications defined in section 2d and for the instant warm-seclusion cases defined in section 2c. For the post-transformation warm-seclusion composite, a storm-centered grid is also generated for the time after  $T_E$  at which the cyclones acquire a warm-seclusion structure. As in H06, no attempt is made to rotate the cyclone-centered grids relative to cyclone motion; thus, any possible sensitivity in structural evolution to cyclone motion is not resolved by this analysis. The cyclone-centered grid used here is smaller than that of H06, which spans 91° latitude and 91° longitude, to avoid situations in which the grid extends beyond the North Pole. H06 handle such cases by filling the grid above the North Pole with missing values, which at times results in variable composite sizes across their analysis grids. Composites involving derived fields are obtained by averaging the derived field over all composite members rather than deriving fields from composite-mean quantities.

#### f. Statistical significance testing

Whereas H06 use a Student's *t* test (Wilks 2006) to evaluate statistical significance, this study evaluates statistical significance using bootstrapping. Relative to the Student's *t* test, bootstrapping has the advantage of providing confidence intervals without assuming how the underlying data are distributed (Efron 1979), ensuring a more-reliable significance evaluation. Bootstrapping

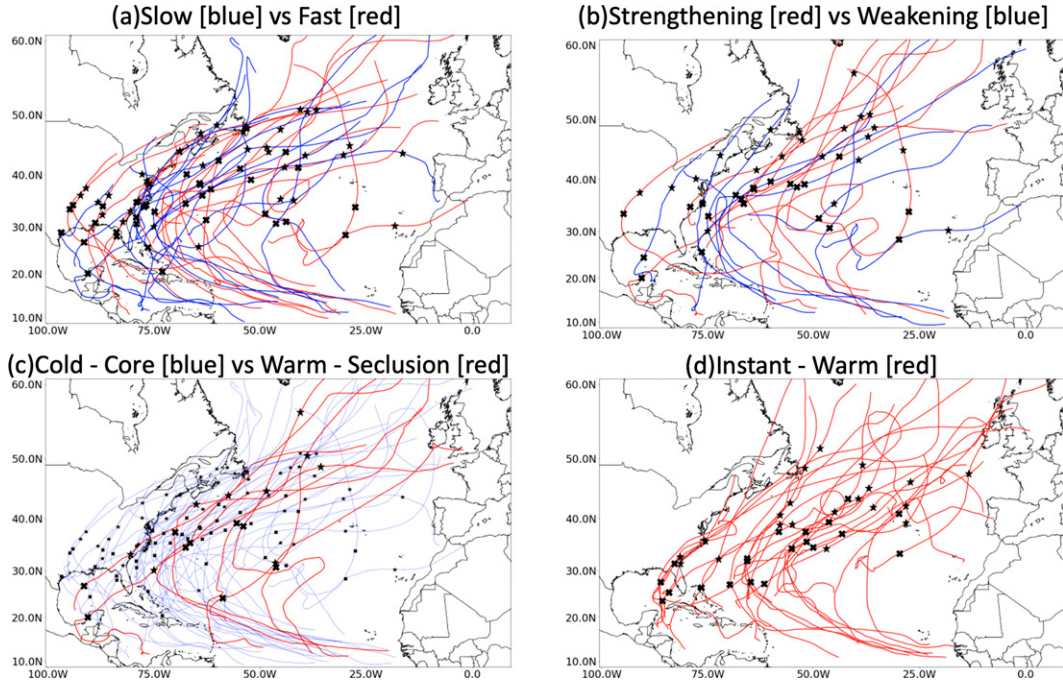


FIG. 3. Lifetime cyclone tracks for (a) slow (red) and fast (blue) ET events, (b) post-transformation strengthening (red) and weakening (blue) ET events, (c) post-transformation warm-seclusion (red) and cold-core (light blue) ET events, and (d) instant warm-seclusion (red) ET events. Crosses indicate cyclone locations at  $T_B$  whereas stars indicate cyclone locations at  $T_E$ ;  $T_E$  is determined using the ERA5-based CPS for all panels except (d), in which  $T_E$  is determined using NHC best track data.

is used to identify the confidence levels at which the composite-mean differences between meteorological features (e.g., an upstream trough or downstream ridge) in the fast and slow transforming, post-transformation strengthening and weakening, post-transformation cold-core and warm-seclusion thermal structure, and instant–warm-seclusion and non-instant warm-seclusion events are significantly different from zero.

To assess the significance of the composite-mean differences between composites with  $M$  and  $N$  TCs at a given milestone, bootstrapping proceeds by first randomly generating 1000 samples of  $M$  and  $N$  TCs at that ET milestone. These 1000 samples are drawn with replacement from the full sample of 78 TCs that undergo ET considered in this study. Next, the composite-mean difference for the composite and ET milestone being considered is compared to those of the 1000 randomly generated samples. The ranking of the composite-mean difference relative to the 1000-member sample determines the resulting significance level. For example, a composite-mean difference that is larger than the 50th-largest (95%) or smaller than the 50th-smallest (5%) difference is said to be significantly different from 0% to  $\geq 90\%$  confidence. Significance is indicated at the 90%, 95%, and 99% confidence levels for synoptic composites and at the 90% and 95% confidence levels for best track–derived composite statistics.

Applied to the synoptic composites, this procedure returns the outcome of *local* (i.e., conducted separately at individual locations) significance tests of a *global* (i.e., over a larger spatial area) null hypothesis. It naively assumes statistical

independence between spatially correlated individual locations, resulting in overstating significance due to inappropriately rejecting the null hypothesis (type-I error) at more locations than is warranted (Wilks 2016). Controlling for the allowable rate of type-I errors (the false discovery rate, or field significance; Benjamini and Hochberg 1995; Wilks 2016) provides one measure of mitigating overstated significance. However, as indicated by Fig. 6a of Wilks (2016), it also increases the rate at which the null hypothesis is inappropriately not rejected (type-II error), often at locations where the significance test's  $p$  value is near its highest values over the analysis domain. For the composites considered in this study, values of the false discovery rate between 2% and 10% typically result in large regions of type-II errors near the regions of highest  $p$  values (not shown). Consequently, we present significance results without controlling for the false discovery rate, albeit with the caveat that these results overstate the spatial coverage and overall presence of significant differences between composites. The primary implication of this choice is that we do not indicate that composite differences are significant at *isolated* locations where the significance test indicates that the differences are significant to at least 90% confidence.

#### *g. Diagnostics*

Four meteorological diagnostics are used to better understand the physical and dynamical contributors to composite differences. First, in support of the comparison between fast- and slow-transforming cyclones, the synoptic-scale environment's

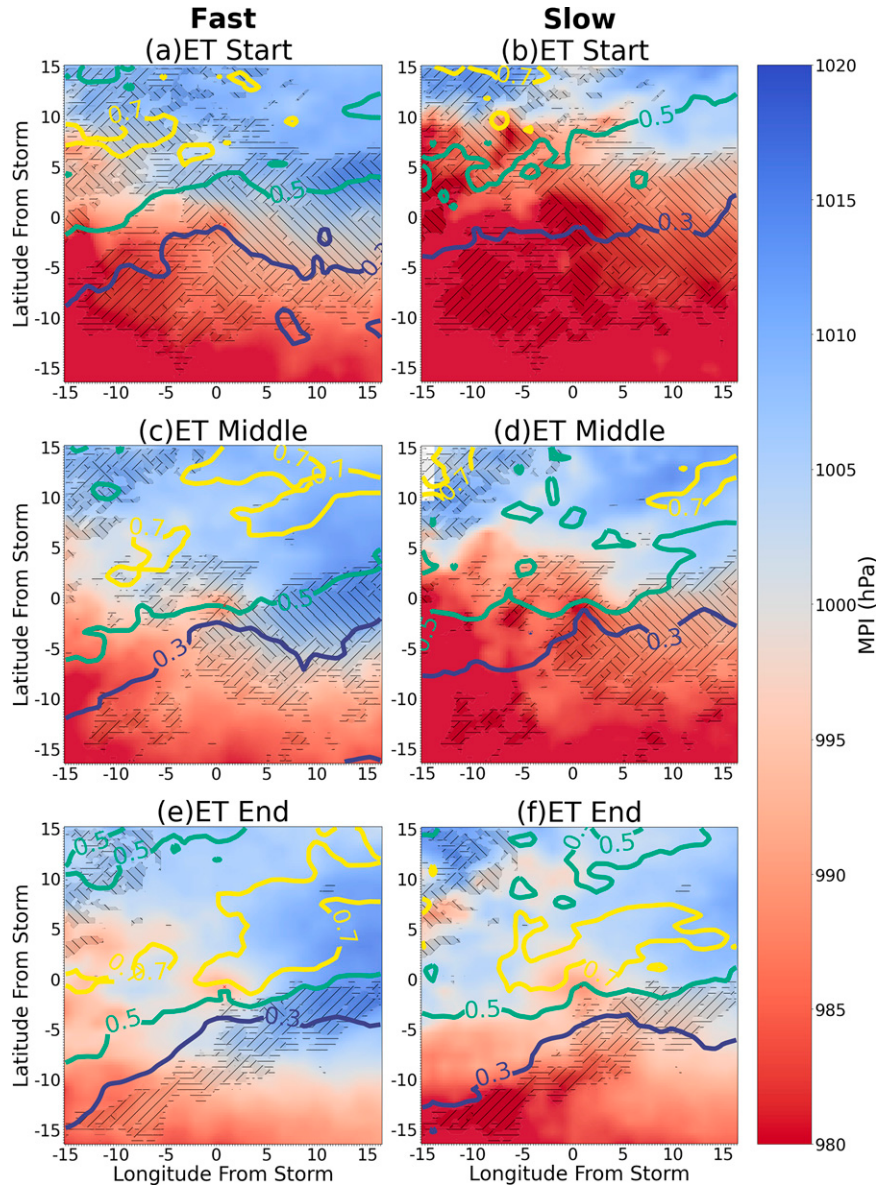


FIG. 4. Composite-mean potential intensity (shaded per the color bar; hPa) and 700-hPa Eady baroclinic growth rate (blue, green, and yellow contours at 0.3, 0.5, and 0.7 day<sup>-1</sup>) for (left) rapidly vs (right) slowly transforming TCs at (a),(b)  $T_B$ ; (c),(d)  $T_{MID}$ ; and (e),(f)  $T_E$ . Hatching indicates regions in which the composite-mean potential intensity fields at a given time are statistically significantly different from each other, as determined using bootstrapping, to 90% (horizontal hatched lines), 95% (positively sloped hatched lines), and 99% (negatively sloped hatched lines) confidence.

ability to support tropical and extratropical cyclone development is assessed using the TC potential intensity (Bister and Emanuel 2002) and Eady baroclinic growth rate (Hoskins and Valdes 1990), respectively. The TC potential intensity represents the theoretical maximum intensity achievable by a TC given the enthalpy that it can gain from the underlying ocean and the efficiency with which this enthalpy can be converted into kinetic energy, whereas the Eady baroclinic growth rate represents the theoretical maximum growth rate of a baroclinically unstable

wave. The overlap, or absence thereof, between regions of high TC potential intensities and large Eady baroclinic growth rates is used by Hart and Evans (2001) to diagnose the climatological likelihood that a recurring TC will complete extratropical transformation and by H06 (with SST substituting for TC potential intensity) to diagnose synoptic-scale conditions favoring fast-versus slow-transforming cyclones.

The TC potential intensity, here given by the minimum sea level pressure at the TC's radius of maximum sustained

TABLE 4. Composite-mean values for cyclone latitude, cyclone longitude, MSLP, translation speed, and the zonal ( $x$ ) and meridional ( $y$ ) components of translation, as derived from NHC best track data, at the ERA5-based CPS-determined  $T_B$ . For the slow vs fast, strengthening vs weakening, and warm-seclusion vs cold-core comparisons, italics and boldface indicate that the respective composite-mean values are significantly different from each other (as determined using bootstrapping) to  $\geq 90\%$  and  $\geq 95\%$  confidence, respectively. For the instant warm-seclusion composite, italics and boldface indicate that the composite-mean value is significantly different from the mean of the 52 ET events that are not instant warm seclusions (as determined using bootstrapping) to  $\geq 90\%$  and  $\geq 95\%$  confidence, respectively.

	No.	Lat (°N)	Lon (°E)	MSLP (hPa)	Translation speed (m s $^{-1}$ )	$x$ direction (m s $^{-1}$ )	$y$ direction (m s $^{-1}$ )
Full composite	78	33.6	-65.4	980.5	8.8	5.4	6.0
Slow	16	<b>30.2</b>	-73.7	981.2	<b>7.0</b>	<b>3.0</b>	<b>4.7</b>
Fast	19	<b>36.0</b>	-64.4	983.2	<b>11.0</b>	<b>7.2</b>	<b>7.4</b>
Strengthening	11	35.8	-64.0	<b>987.5</b>	8.2	5.4	7.2
Weakening	10	32.5	-62.7	<b>963.9</b>	9.4	6.0	6.2
Warm seclusion	9	31.9	-66.8	983.4	8.7	5.7	6.2
Cold core	43	34.5	-68.7	981.7	8.9	5.3	6.0
IW	26	32.8	<b>-59.5</b>	977.4	8.6	5.3	5.9

surface winds  $p_{RMW}$ , is computed using the pyPI (Gilford 2021) Python package and is given by (Bister and Emanuel 2002):

$$R_D T_v \ln\left(\frac{p_0}{p_{RMW}}\right) = \frac{1}{2} V_{\max}^2 + \text{CAPE}_{\text{env}},$$

where  $V_{\max}^2 = (T_s/T_o)(C_K/C_D)(\text{CAPE}^* - \text{CAPE}_{\text{env}})$ ,  $T_s$  is the ambient surface virtual temperature,  $p_o$  is the ambient sea level pressure,  $\text{CAPE}_{\text{env}}$  is the ambient surface-based CAPE,  $\text{CAPE}^*$  is the ambient surface-based CAPE of a saturated air parcel,  $T_s$  is the ambient surface temperature,  $T_o$  is the ambient TC outflow-layer temperature,  $C_K$  is the surface enthalpy exchange coefficient, and  $C_D$  is the momentum drag coefficient.

The Eady baroclinic growth rate  $\sigma$ , here computed at 700 hPa, is given by (Hoskins and Valdes 1990):

$$\sigma = 0.31f \left\| \frac{\partial \mathbf{v}}{\partial z} \right\| N^{-1},$$

where  $f$  is the Coriolis parameter,  $\|\partial \mathbf{v} / \partial z\|$  is the vertical wind shear magnitude, and  $N$  is the Brunt–Väisälä frequency.

Next, in support of the comparison between post-transformation intensifying versus weakening cyclones, phasing between transforming TCs and an upstream trough is quantified using the 250–150-hPa layer-mean negative PV advection by the irrotational wind (Archambault et al. 2013, 2015):

$$-\mathbf{v}_\chi \cdot \nabla \text{PV} < 0,$$

where  $\chi$  is the irrotational wind and is calculated using the windspharm (Dawson 2016) Python package. More-negative values of this diagnostic indicate greater phasing between a transforming TC and upstream trough, characterized by strong upper-tropospheric divergent outflow from the transforming TC directed perpendicular to the eastern (or leading) edge of the upper-tropospheric PV gradient associated with the upstream trough.

Finally, in support of the comparison between post-transforming cold-core and warm-seclusion cyclones and the analysis of instant warm-seclusion cyclones, lower-tropospheric frontal

structural evolution during ET is assessed using the 850-hPa kinematic frontogenesis  $F$  (Bluestein 1993),

$$F = \frac{1}{2} \|\nabla \theta\| [D \cos(2\beta) - \delta],$$

where  $D$  is the total (stretching plus shearing) deformation,  $\beta$  is the local angle between the axis of dilatation and the isentropes, and  $\delta$  is divergence. Frontogenesis  $F$  is computed using the Metpy (May et al. 2022) Python package. Positive values of this diagnostic indicate a local increase in the magnitude of the horizontal potential-temperature gradient.

### 3. Factors distinguishing post-transformation extremes

The analysis in this section focuses only on the 52 TCs listed in Table 2 for which reliable ET milestones are identifiable within the ERA5-based CPS. Note that although each TC is found in multiple composites (Table 2), the proportions of slow and fast transforming, post-transformation strengthening and weakening, and post-transformation cold-core and warm-seclusion TCs within the full 52-case sample are approximately maintained within each composite (except for fast-transforming TCs, none of which are post-transformation warm-seclusion cyclones). In other words, there is minimal correspondence between composites. Thus, the associated analyses are believed to be unique to each composite.

In the analyses that follow, three times from the normalized ET timeline are shown for each composite. This expands upon H06, which considered only one time per composite for all analyses except their Eliassen–Palm–flux analysis. The selected times represent the period of greatest interest for each comparison, which is generally also when the composite differences are largest and most significant. For transformation-stage duration, which encapsulates the period between  $T_B$  and  $T_E$ , analyses are presented at  $T_B$ ,  $T_{\text{MID}}$ , and  $T_E$ . For post-transformation intensity-change and thermal structure, for which the definitions extend to  $T_E + 24$  h or beyond, analyses are presented at  $T_{\text{MID}}$ ,  $T_E$ , and  $T_E + 24$  h.

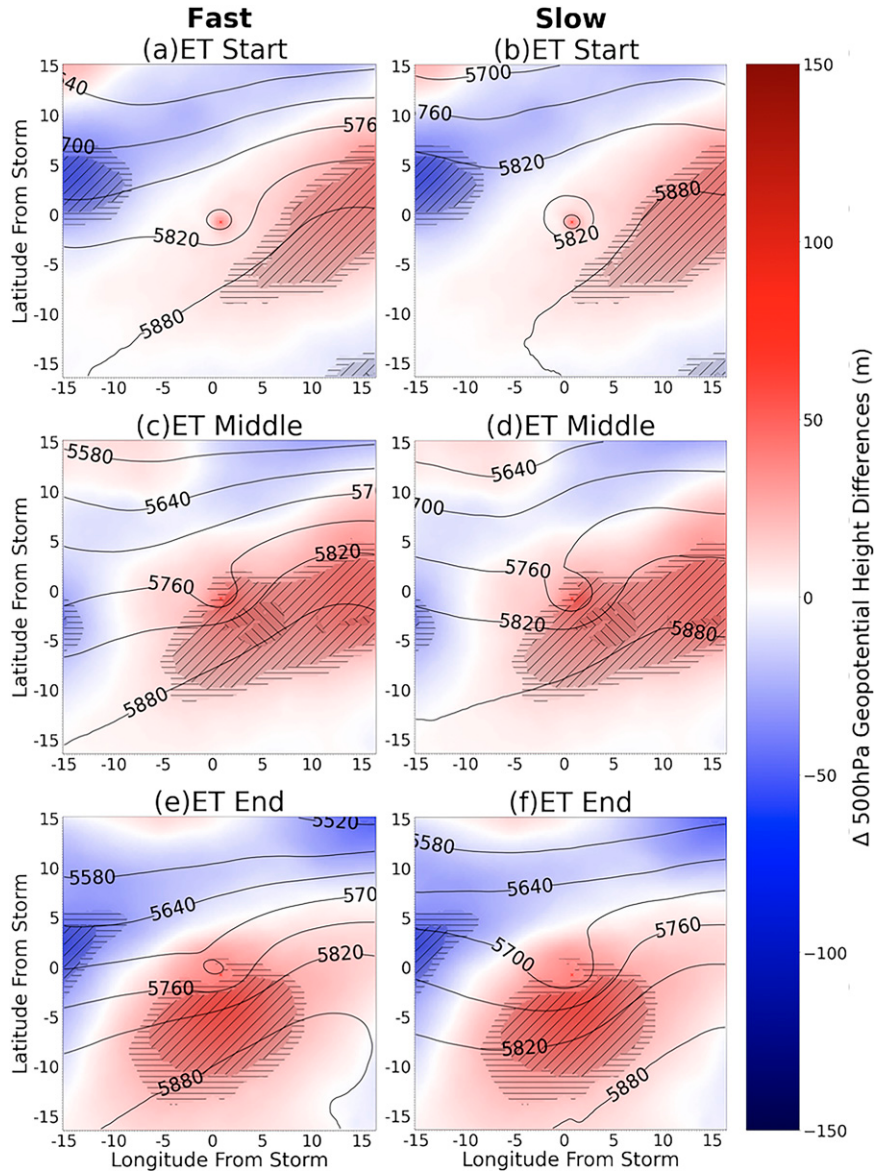


FIG. 5. Composite-mean 500-hPa geopotential height (black contours every 60 m) and composite-mean 500-hPa geopotential height difference (defined as rapidly minus slowly transforming composite means; shaded per the color bar in meters) for (left) rapidly vs (right) slowly transforming TCs at (a),(b)  $T_B$ ; (c),(d)  $T_{MID}$ ; and (e),(f)  $T_E$ . Hatching indicates regions in which the composite-mean 500-hPa geopotential height difference at a given time is statistically significantly different from zero, as determined using bootstrapping, to 90% (horizontal hatched lines), 95% (positively sloped hatched lines), and 99% (negatively sloped hatched lines) confidence.

#### a. Rapidly versus slowly transforming events

Both rapidly and slowly transforming TCs enter regions permissive of baroclinic development, with lower- to midtropospheric Eady baroclinic growth rates exceeding  $0.5 \text{ day}^{-1}$ , between  $T_B$  and  $T_{MID}$  (Fig. 4). However, rapidly transforming TCs begin transformation at significantly higher latitudes (to  $\geq 95\%$  confidence; Table 4) over colder SSTs (not shown) with significantly weaker potential intensity (to  $\geq 95\%-99\%$

confidence; Figs. 4a,b). Further, these rapidly transforming TCs also move significantly faster to the north and east during transformation within a significantly more amplified (to  $\geq 95\%$  confidence) synoptic-scale pattern (characterized by a deeper upstream trough and more-amplified downstream ridge beginning at  $T_B$ , with this flow configuration persisting at approximately the same amplitude and significance through  $T_E$ ; Fig. 5). Thus, rapidly transforming TCs quickly move

TABLE 5. As in Table 4, but at  $T_E + 24$  h. The numbers in parentheses in the MSLP (hPa) column for the strengthening and weakening composites indicate the 24-h intensity change between  $T_E + 24$  h and  $T_E$ , defined as  $\text{MSLP}_{T_E+24\text{h}} - \text{MSLP}_{T_E}$ , for each composite.

	No.	Lat ( $^{\circ}\text{N}$ )	Lon ( $^{\circ}\text{E}$ )	MSLP (hPa)	Translation speed ( $\text{m s}^{-1}$ )	$x$ direction ( $\text{m s}^{-1}$ )	$y$ direction ( $\text{m s}^{-1}$ )
Full composite	78	47.7	-43.9	988.3	13.8	10.0	7.1
Slow	16	45.2	-51.4	995.8	12.9	9.4	7.0
Fast	19	48.2	-43.3	997.8	17.2	13.2	7.3
Strengthening	11	53.6	-39.0	981.9 (-6.7)	16.9	10.2	8.9
Weakening	10	48.7	-39.3	994.8 (17)	15.1	11.9	7.3
Warm seclusion	9	48.1	-39.9	983.9	16.8	15.2	6.0
Cold core	43	48.0	-46.8	995.4	14.2	10.1	7.5
IW	26	47.15	-41.0	978.0	11.9	8.0	7.0

during the transformation stage from regions of warm SSTs and deeper potential intensities to strongly baroclinic regions characterized by cold SSTs and weak potential intensities (Hart and Evans 2001; H06). Conversely, slowly transforming TCs remain in regions of comparatively warm SSTs and deeper potential intensities even after encountering strong baroclinicity, mitigating the rate at which extratropical cyclone structure develops (Ritchie and Elsberry 2003; H06). These findings are consistent with H06's transformation-stage duration analysis.

Rapidly and slowly transforming TCs are also distinguished by when during the North Atlantic TC season they preferentially occur. Rapidly transforming TCs preferentially occur prior to the TC season's peak, with 10 of 19 rapidly transforming TCs occurring in June, July, and August. Conversely, slowly transforming TCs preferentially occur after the TC season's peak, with 14 of 16 slowly transforming TCs occurring in September, October, and November. These differences stem from seasonal differences in the oceanic and atmospheric climatologies of the North Atlantic basin. Specifically, slowly transforming TCs are favored later in the North Atlantic TC season as this is when regions where the Eady baroclinic growth rate is supportive of baroclinic development best overlap with regions where the potential intensity is sufficient warm as to support tropical development (Hart and Evans 2001, their Fig. 7). This overlap is facilitated primarily by the seasonal equatorward movement of regions where the Eady baroclinic growth rate is supportive of baroclinic development and is thus consistent with slowly transforming TCs occurring at significantly lower latitudes (to  $\geq 95\%$  confidence; Table 4) as compared to their rapidly transforming counterparts.

#### b. Post-transformation strengthening versus weakening cases

The intensity evolutions of post-transformation strengthening and weakening cyclones are significantly different during and after extratropical transformation. Post-transformation weakening cyclones have significantly lower MSLP than post-transformation strengthening cyclones at  $T_B$  ( $\geq 95\%$  confidence, with  $\Delta p = -23.6$  hPa; Table 4), remain stronger through  $T_E$  (Table 5), and have significantly higher MSLP at  $T_E + 24$  h (to  $\geq 95\%$  confidence, with  $\Delta p = +12.9$  hPa; Table 5). The significantly lower MSLP of the post-transformation weakening cyclones during the transformation stage is facilitated, at least

through  $T_{\text{MID}}$ , by significantly higher SSTs (not shown) and, consequently, larger potential intensities in an increasingly baroclinic environment (Figs. 6a,b). Notably, the post-transformation weakening cyclones' composite-mean MSLP at  $T_E$  (977.8 hPa; Table 5) is within the lowest quintile of the MSLP distribution of Northern Hemisphere wintertime extratropical cyclones (e.g., Fig. 3a of Neu et al. 2013), suggesting that these initially intense TCs are climatologically likely to weaken following transformation absent substantial baroclinic forcing.

The composite-mean synoptic patterns associated with post-transformation strengthening and weakening cyclones are significantly different during and after extratropical transformation. Post-transformation strengthening cyclones are embedded within a significantly more amplified synoptic pattern as compared to post-transformation weakening cyclones, as characterized by a significantly stronger downstream ridge at  $T_{\text{MID}}$  (to  $\geq 95\%$  confidence; Figs. 7a,b), significantly stronger subtropical anticyclone to the south at  $T_{\text{MID}}$  and  $T_E$  (to  $\geq 99\%$  confidence; Figs. 7a–d), and significantly stronger upstream trough at  $T_E + 24$  h (to  $\geq 99\%$  confidence; Figs. 7e,f). Consistent with H06, the upstream trough becomes negatively tilted in the post-transformation strengthening composite after  $T_E$  (Figs. 7e,f). In contrast to H06 and other studies (Thornicroft and Jones 2000; Hart and Evans 2001; Ritchie and Elsberry 2003, 2007), however, post-transformation strengthening cyclones are not embedded within a warmer, moister lower-tropospheric air mass during or following transformation (Fig. 8).

The substantial changes between  $T_E$  and  $T_E + 24$  h in the post-transformation strengthening and weakening composite-mean cyclone intensities and synoptic patterns are the result of improved phasing (Klein et al. 2002; Ritchie and Elsberry 2003, 2007) between post-transformation strengthening cyclones and their upstream troughs following  $T_E$ , as characterized by larger upper-tropospheric negative PV advection by the irrotational wind (Figs. 9c,d; Archambault et al. 2013, 2015). This improved phasing results in larger midtropospheric cyclonic relative-vorticity advection atop the cyclone (Figs. 9c,d), larger lower- to midtropospheric warm-air advection atop and downstream from the cyclone (Figs. 9c,d), and significantly reduced lower-tropospheric equivalent potential temperature (associated with cold-air advection; not shown) in the base of the upstream trough (to  $\geq 95\%$  confidence; Figs. 8e,f). These attributes are consistent with the "self-development" paradigm for extratropical

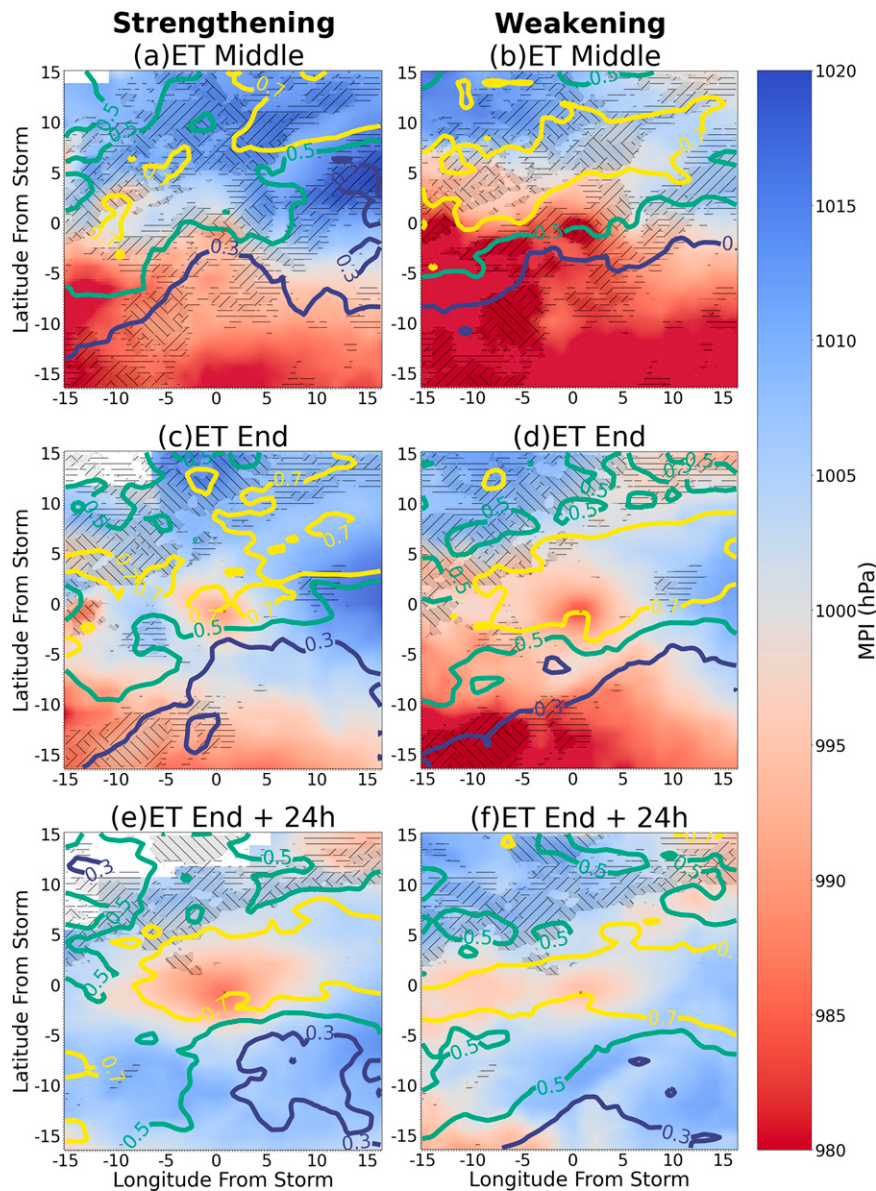


FIG. 6. Composite-mean potential intensity (shaded per the color bar; hPa) and 700-hPa Eady baroclinic growth rate (blue, green, and yellow contours at  $0.3, 0.5$ , and  $0.7 \text{ day}^{-1}$ ) for post-transformation (left) strengthening vs (right) weakening cyclones at (a),(b)  $T_{\text{MID}}$ ; (c),(d)  $T_E$ ; and (e),(f)  $T_E + 24 \text{ h}$ . Hatching indicates regions in which the composite-mean potential intensity fields at a given time are statistically significantly different from each other, as determined using bootstrapping, to 90% (horizontal hatched lines), 95% (positively sloped hatched lines), and 99% (negatively sloped hatched lines) confidence.

cyclogenesis (Sutcliffe and Forsdyke 1950; Pettersen 1955). Additionally, post-transformation strengthening cyclones are located within the right entrance region of a downstream upper-tropospheric jet and the left exit region of an upstream upper-tropospheric jet (Fig. 10e), the latter of which intensifies between  $T_E$  and  $T_E + 24 \text{ h}$  in response to upper-tropospheric positive PV advection by the irrotational wind in the base of the upstream trough (Fig. 9c), coinciding with ageostrophic forcing for midtropospheric ascent and a favored location for post-

transformation cyclone intensification (Harr et al. 2000; Harr and Elsberry 2000; Klein et al. 2002; Kitabatake 2008).

Summarizing, whereas post-transformation weakening cyclones are more intense through  $T_E$  in association with warmer SSTs and higher potential intensities, post-transformation strengthening cyclones become more intense after  $T_E$  owing to improved phasing between the cyclone and upstream trough. Notably, the composite-mean lower- to midtropospheric thermal (Figs. 8 and 9) and mid- to upper-tropospheric dynamical

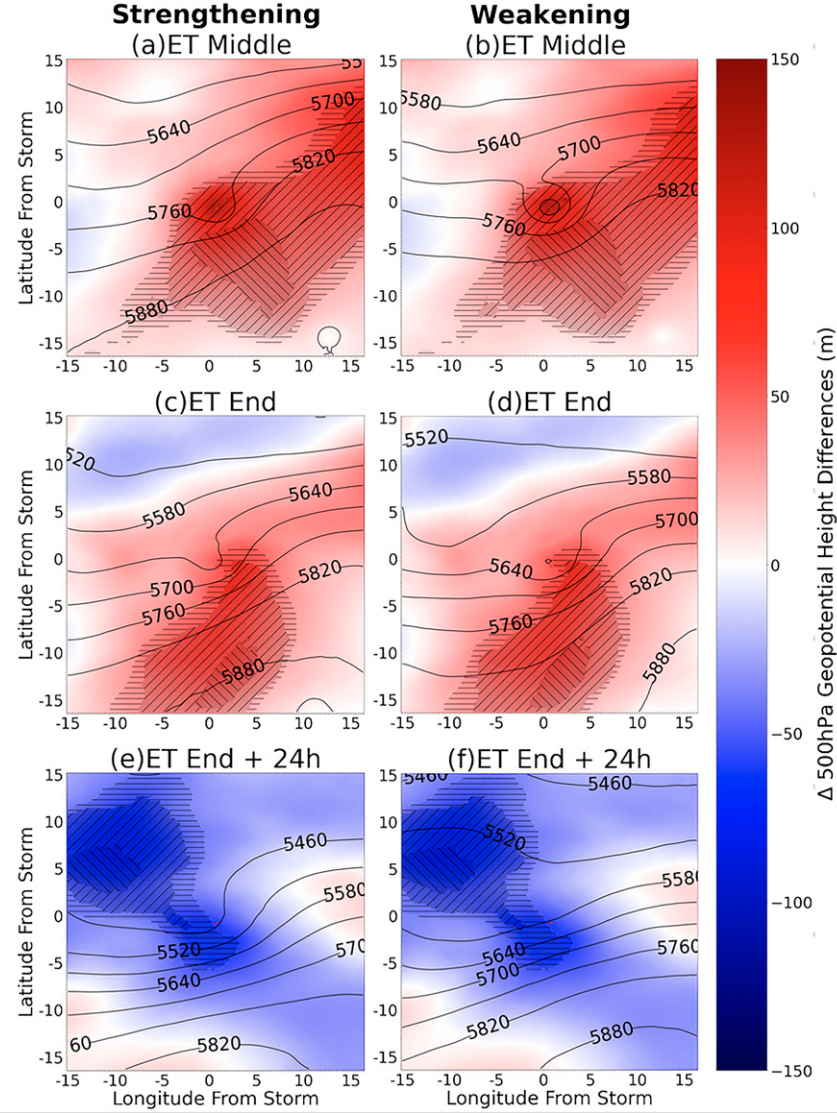


FIG. 7. Composite-mean 500-hPa geopotential height (black contours every 60 m) and composite-mean 500-hPa geopotential height difference (defined as post-transformation strengthening minus weakening composite means; shaded per the color bar; m) for post-transformation (left) strengthening vs (right) weakening TCs at (a),(b)  $T_{\text{MID}}$ ; (c),(d)  $T_E$ ; and (e),(f)  $T_E + 24$  h. Hatching indicates regions in which the composite-mean 500-hPa geopotential height difference at a given time is statistically significantly different from zero, as determined using bootstrapping, to 90% (horizontal hatched lines), 95% (positively sloped hatched lines), and 99% (negatively sloped hatched lines) confidence.

(Figs. 9 and 10) fields are generally similar between the post-transformation strengthening and weakening composites through  $T_E$ , underscoring the importance of phasing after  $T_E$  in determining post-transformation cyclone intensity. As in H06, the post-transformation strengthening composite is characterized by a negatively tilted upstream trough (Fig. 7e). However, consistent with Ritchie and Elsberry (2003, 2007), the upstream trough's negative tilt appears to be an outcome rather than a leading indicator of phasing since the trough is not negatively tilted through  $T_E$  (Fig. 7c). Specifically, persistent tropospheric-deep diabatic warming near the center of the

post-transformation strengthening cyclones redistributes lower-PV air to the upper troposphere, whereupon the cyclones' divergent outflow advects this lower-PV air northwestward against the upstream trough's northeastern flank (Fig. 9c), slowing its eastward progression relative to the trough's base and thus facilitating negative-tilt development (Figs. 7e and 10e).

#### c. Post-transformation warm seclusions versus cold-core cases

Apart from a slightly but significantly stronger (to  $\geq 90\%$  confidence) upstream trough in the post-transformation warm-

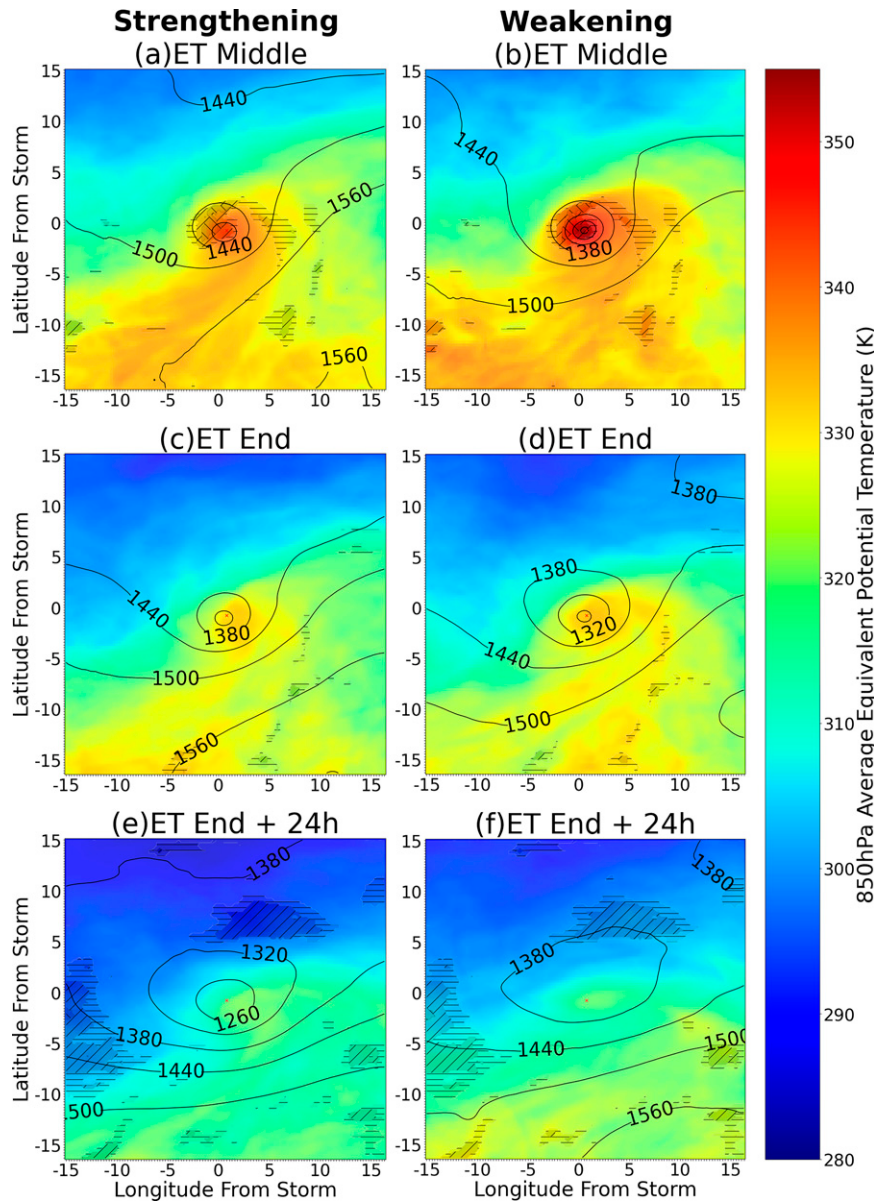


FIG. 8. Composite-mean 850-hPa geopotential height (black contours every 60 m) and 850-hPa equivalent potential temperature (shaded per the color bar; K) for post-transformation (left) strengthening and (right) weakening TCs at (a),(b)  $T_{\text{MID}}$ ; (c),(d)  $T_E$ ; and (e),(f)  $T_E + 24 \text{ h}$ . Hatching indicates regions in which the composite-mean 850-hPa equivalent potential temperature fields at a given time are statistically significantly different from each other, as determined using bootstrapping, to 90% (horizontal hatched lines), 95% (positively sloped hatched lines), and 99% (negatively sloped hatched lines) confidence.

seclusion composite at  $T_{\text{MID}}$  (Figs. 11a,b), the near-field and upstream synoptic environments are not significantly different among post-transformation cold-core and warm-seclusion cyclones (Figs. 11a,b,d,e,g,h). Their downstream environments are significantly different, however, with post-transformation warm-seclusion cyclones moving into strongly confluent flow associated with a significantly stronger (to  $\geq 90\%$  confidence) trough  $\sim 2000$  km to their northeast at and after  $T_E$  (Figs. 11d,e,g,h). The translation of post-transformation warm-seclusion cyclones into

this synoptic environment is associated with significantly larger lower-tropospheric frontogenesis (to  $\geq 90\%$  confidence) along their warm and bent-back fronts and significantly larger lower-tropospheric frontolysis (to  $\geq 90\%$  confidence) along the northernmost extent of their cold fronts (Figs. 12a,b,d,e,g,h and 13c). This results in cold-frontal fracture and warm-seclusion structure development (Fig. 13b), consistent with Schultz et al. (1998) and Schultz and Zhang (2007). Notably, H06's post-transformation warm-seclusion composite is also

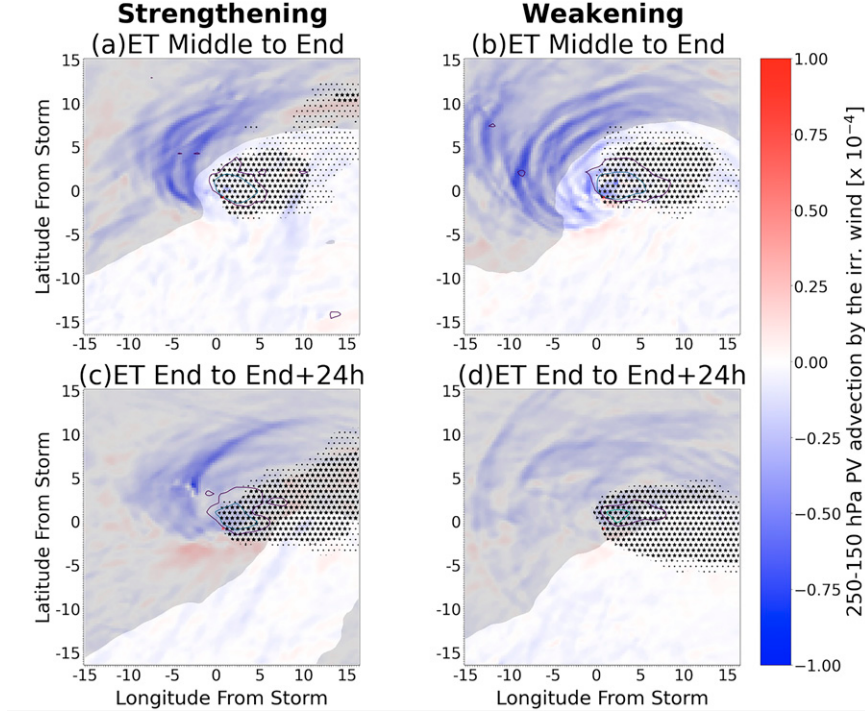


FIG. 9. Composite-mean 250–150-hPa layer-mean PV [partially transparent gray shading at 2 PVU ( $1 \text{ PVU} = 1 \times 10^{-6} \text{ m}^2 \text{ s}^{-1} \text{ K} \text{ kg}^{-1}$ )], 250–150-hPa layer-mean PV advection by the irrotational wind (shaded per the color bar;  $\times 10^{-4} \text{ PVU s}^{-1}$ , such that  $0.23 \times 10^{-4} \text{ PVU s}^{-1} = 2 \text{ PVU day}^{-1}$ ), 700–500-hPa layer-mean relative-vorticity advection (purple contours at  $2 \times 10^{-9} \text{ s}^{-2}$  and  $5 \times 10^{-9} \text{ s}^{-2}$ ), and 850–700-hPa layer-mean potential-temperature advection (dots at  $3 \times 10^{-5} \text{ K s}^{-1}$  and stars at  $5 \times 10^{-5} \text{ K s}^{-1}$ ) for post-transformation (left) strengthening and (right) weakening TCs averaged between (a),(b)  $T_{\text{MID}}$  and  $T_E$  and (c),(d)  $T_E$  and  $T_E + 24 \text{ h}$ .

characterized by strongly confluent downstream flow associated with a significantly stronger trough  $\sim 2000$  km to the northeast (H06, their Figs. 14b and 15c), but the potential role of this environment in facilitating post-transformation warm-seclusion structural development is not discussed by H06.

Unlike H06, post-transformation warm-seclusion cyclones are not associated with a narrower upstream trough than their post-transformation cold-core counterparts, whether in the mid (Figs. 11a,b,d,e,g,h and 13a) or upper troposphere (Figs. 14a,b,d,e,g,h). Although there is stronger upper-tropospheric negative PV advection by the irrotational wind against the upstream trough's eastern flank in the post-transformation warm-seclusion composite after  $T_{\text{MID}}$  (Figs. 14d,e,g,h), in a composite-mean sense this appears to facilitate the local cyclonic rollup of the upper-tropospheric PV surfaces rather than cause the upstream trough—the axis of which remains  $10^\circ$  longitude upstream of the post-transformation cyclones through  $T_E + 24 \text{ h}$  (Fig. 11h)—to narrow to match the scale of the transforming cyclones. This is not to say that the upstream trough does not narrow with some post-transformation warm-seclusion cyclones (such as the subset considered by H06), but rather that it does not appear to be as essential for warm-seclusion structural development as is the cyclones' movement into a strongly confluent synoptic

environment (Schultz et al. 1998; Schultz and Zhang 2007). As indicated by H06, further investigation remains necessary to diagnose how scale matching between a transforming cyclone and narrowing upstream trough can facilitate post-transformation warm-seclusion structural development (and not just focused and intensified quasigeostrophic forcing for midtropospheric ascent, as in Molinari et al. 1998; Bracken and Bosart 1998; Bosart et al. 2000).

#### 4. Instant warm-seclusion cyclones

As North Atlantic Ocean instant warm-seclusion cyclones are hitherto understudied, at least in a composite sense, we begin by presenting a brief climatology of these cyclones. Instant warm-seclusion cyclones are most common in October and November (not shown), at which times they account for nearly half of all ET events and 20%–25% of all TCs. Like post-transformation warm-seclusion cyclones (Fig. 3c), instant warm-seclusion cyclones primarily occur over water (Fig. 3d). This is consistent with prior studies which suggest that the reduced frictional convergence and larger upward-directed surface sensible and latent heat fluxes over water relative to land are necessary for extratropical warm-seclusion development (e.g., Kuo et al. 1992; Mass and Schultz 1993; Hines and Mechoso 1993). Furthermore, consistent with the seclusion-occlusion cyclones

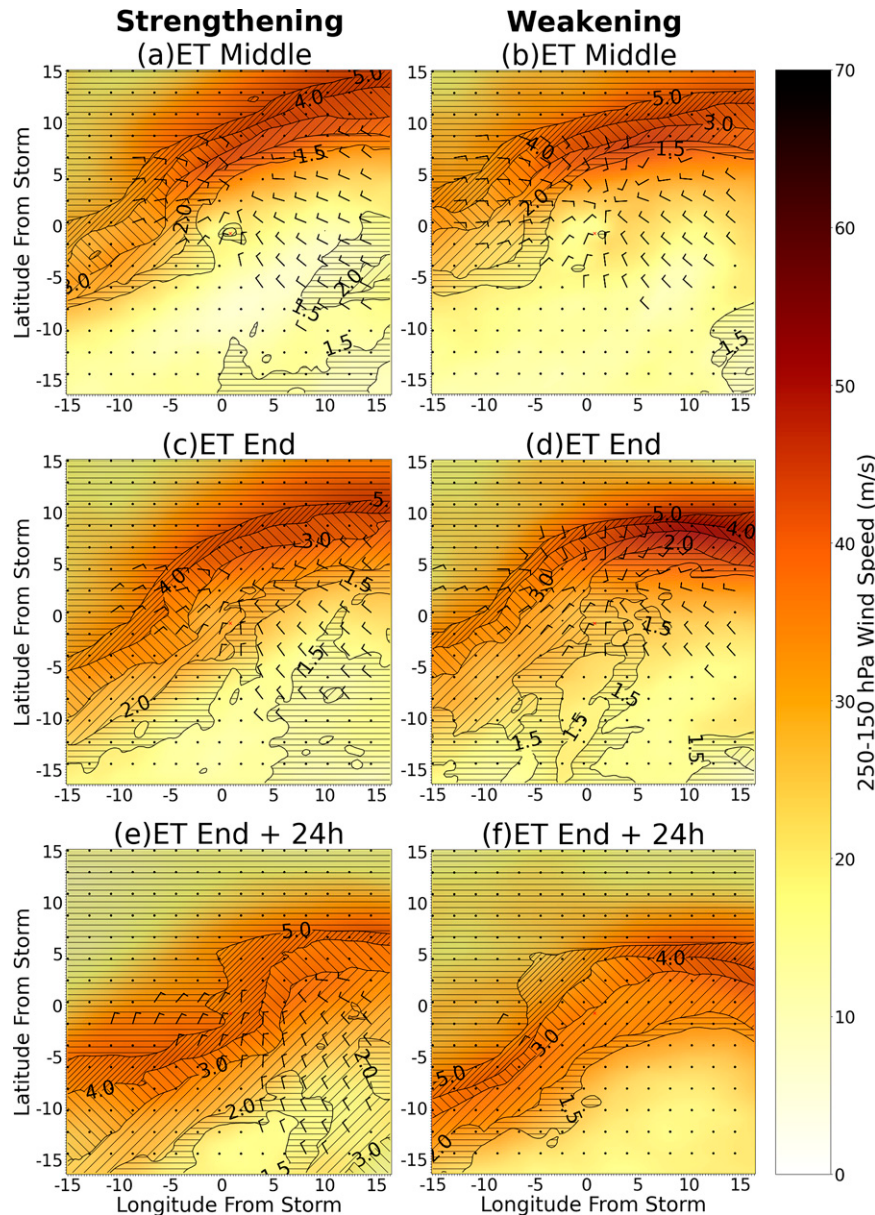


FIG. 10. Composite-mean 250–150-hPa layer-mean PV (contours and hatching at 1.5, 2, 3, 4, and 5 PVU), 250–150-hPa layer-mean horizontal wind speed (shaded per the color bar;  $\text{m s}^{-1}$ ), and 250–150-hPa layer-mean irrotational wind (black bars at  $5 \text{ m s}^{-1}$ ) for post-transformation (left) strengthening vs (right) weakening TCs at (a),(b)  $T_{\text{MID}}$ ; (c),(d)  $T_E$ ; and (e),(f)  $T_E + 24 \text{ h}$ .

(Kitabatake 2008) with which they share many structural similarities, instant warm-seclusion cyclones are significantly more intense (to  $\geq 95\%$  confidence) following transformation than other post-transformation cyclones (Table 5). Finally, instant warm-seclusion cyclones move significantly slower (to  $\geq 95\%$  confidence) following transformation, particularly zonally (consistent with Kitabatake 2008), than do other post-transformation cyclones (Table 5).

Instant warm-seclusion events are characterized by the upstream trough–cyclone pair becoming negatively tilted (from

northwest to southeast) and undergoing cyclonic Rossby wave breaking (the LC2 synoptic life cycle of Thorncroft et al. 1993; Figs. 11c,f,i) as it approaches the midlatitude jet's right-entrance region. This process is accompanied in the lower troposphere by significant (to  $\geq 95\%$  confidence) frontogenesis along a bent-back front (Shapiro and Keyser 1990) poleward and frontolysis near and southwest of the transforming cyclone (Figs. 13c,f,i), facilitating the cyclone's seclusion within relatively warm, moist lower-tropospheric air (not shown). These characteristics are shared by the seclusion–occlusion

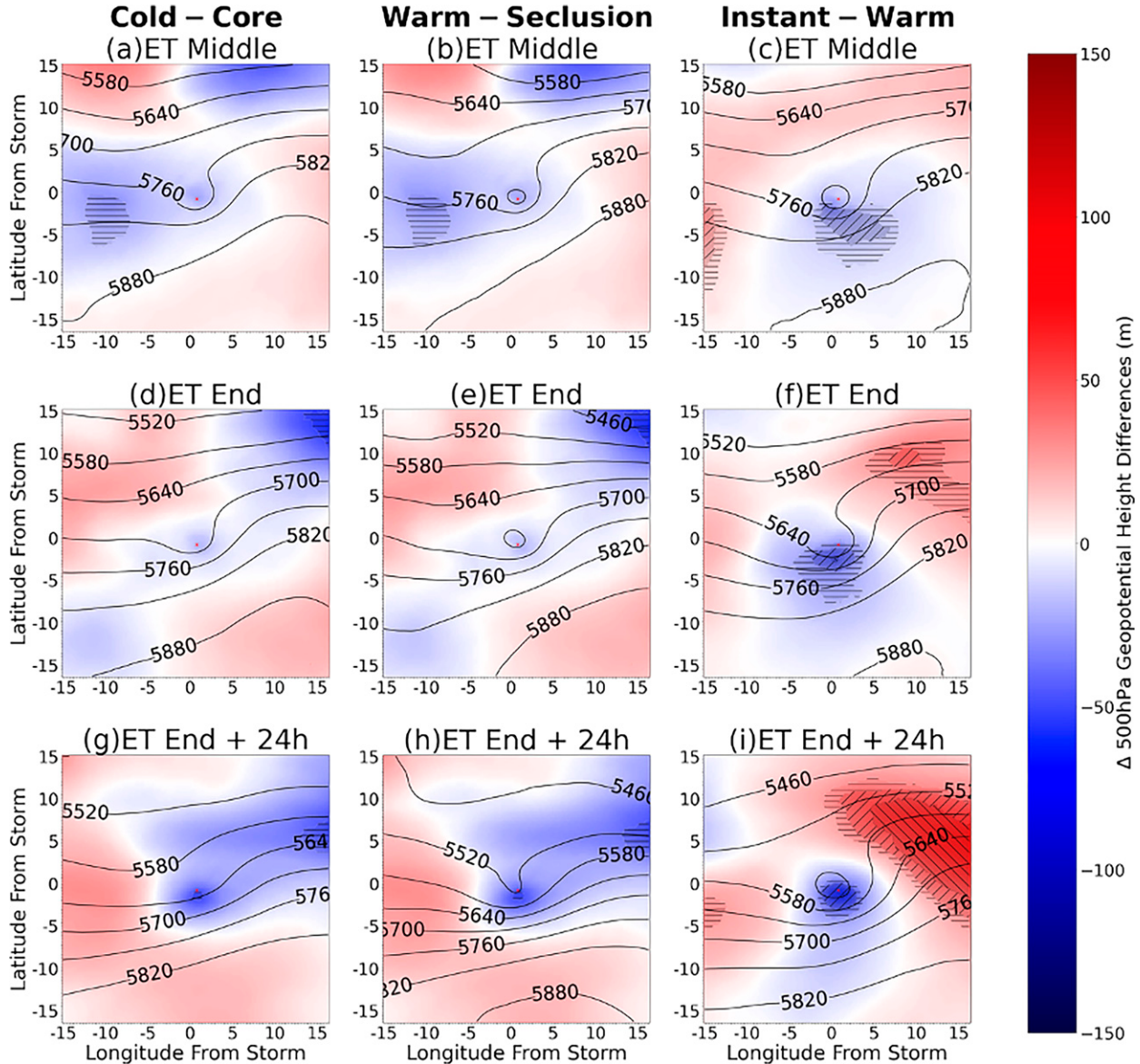


FIG. 11. Composite-mean 500-hPa geopotential height (black contours every 60 m) and composite-mean 500-hPa geopotential height difference (defined as post-transformation warm-seclusion minus cold-core composite means; shaded per the color bar; m) for the post-transformation (left) cold-core vs (center) warm-seclusion TCs at (a),(b)  $T_{\text{MID}}$ ; (c),(d)  $T_E$ ; and (e),(f)  $T_E + 24$  h. Hatchling indicates regions in which the composite-mean 500-hPa geopotential height difference at a given time is statistically significantly different from zero, as determined using bootstrapping, to 90% (horizontal hatched lines), 95% (positively sloped hatched lines), and 99% (negatively sloped hatched lines) confidence. (right) As at center, but for instant rather than post-transformation warm seclusions, with composite-mean differences and the statistical significance thereof computed relative to the respective 52-event non-instant warm-seclusion composite mean.

cyclones studied by Kitabatake (2008), lending confidence that the instant warm-seclusion classification is not an artifact of the classification methods used in this study.

To first order, the instant warm-seclusion composite-mean synoptic environment appears to be somewhat more conducive to cyclonic Rossby wave breaking than other post-transformation composite-mean environments. Specifically, instant warm-seclusion cyclones move significantly slower than other transforming cyclones (to  $\geq 95\%$  confidence; Table 5) and are

associated with a comparatively weak upper-tropospheric jet stream (Figs. 14c,f,i), both of which are consistent with cyclonic Rossby wave breaking occurring when the Rossby wave's phase speed slows to match that of the relatively weak flow within which it is embedded (Polvani et al. 1989; Polvani and Plumb 1992; Swanson et al. 1997). However, instant warm-seclusion cyclones (Tables 4 and 5) and their associated upper-tropospheric jet streams (Figs. 14c,f,i) are not at significantly lower latitudes than other post-transformation cyclones, which

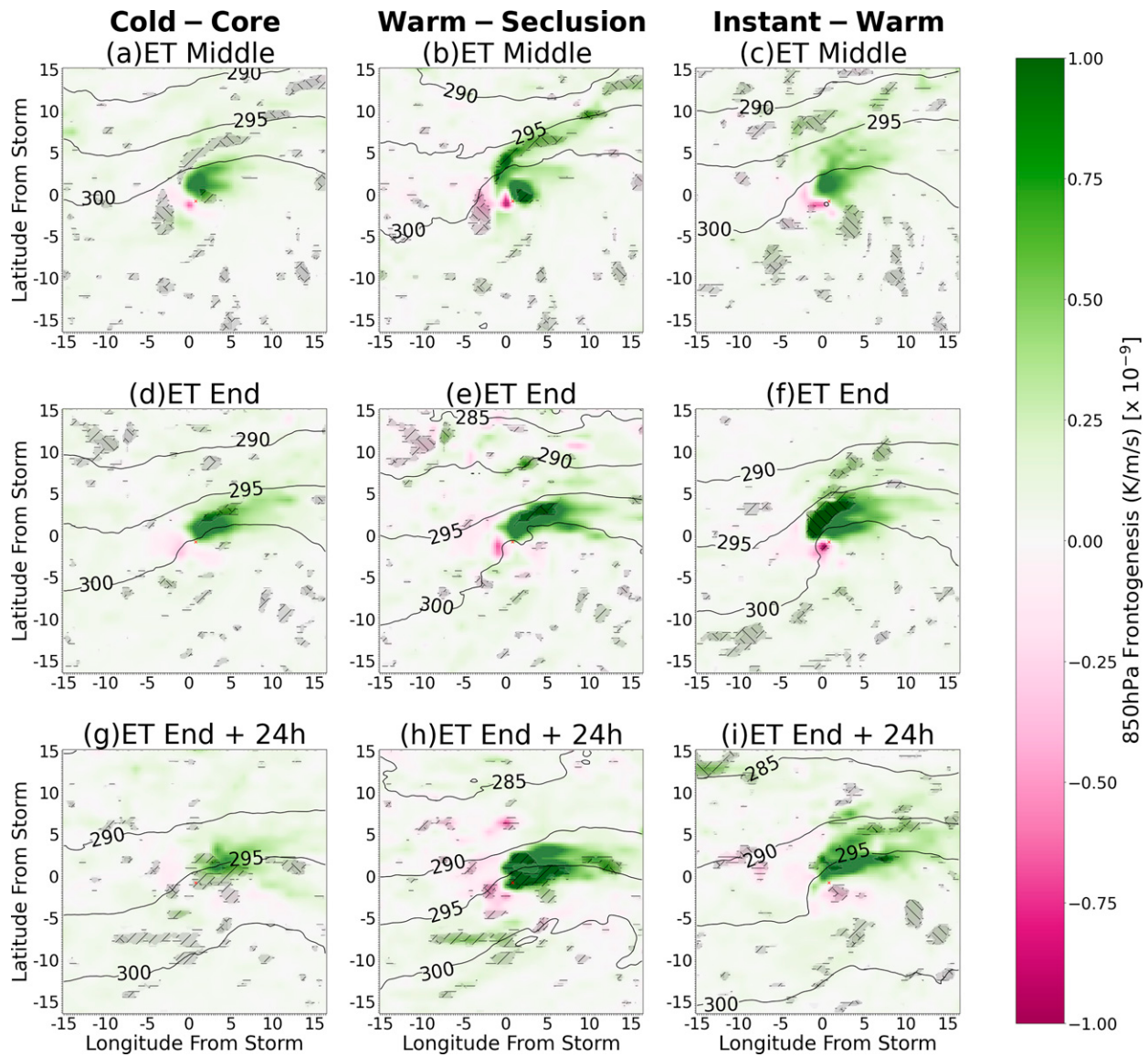


FIG. 12.  $1^{\circ}$  smoothed composite-mean 850-hPa potential temperature (black contours every 5 K) and 850-hPa two-dimensional kinematic frontogenesis (shaded per the color bar;  $\times 10^{-9} \text{ K m}^{-1} \text{ s}^{-1}$ ) for the post-transformation (left) cold-core; (center) warm-seclusion; and (right) instant warm-seclusion composites at (a)–(c)  $T_{\text{MID}}$ ; (d)–(f)  $T_E$ ; and (g)–(i)  $T_E + 24 \text{ h}$ . Hatching in the first two columns indicates regions in which the composite-mean 850-hPa two-dimensional kinematic frontogenesis fields for the cold-core and warm-seclusion composites at a given time are statistically significantly different from each other, as determined using bootstrapping, to 90% (horizontal hatched lines), 95% (positively sloped hatched lines), and 99% (negatively sloped hatched lines) confidence. Hatching for the instant warm-seclusion composites indicates where the composite-mean 850-hPa two-dimensional kinematic frontogenesis is significantly different from the respective 52-event non-instant warm-seclusion composite mean.

is not necessarily consistent with cyclonic Rossby wave breaking's tendency to occur with anomalously equatorward-displaced jets (e.g., Schultz et al. 2019).

## 5. Summary and discussion

Motivated in part by case studies of post-transformation intensity change that do not comport with H06's post-transformation intensity-change composite analysis (as discussed in section 5b of

Evans et al. 2017), this study updates H06's transformation-stage duration, post-transformation intensity change, and post-transformation thermal structural composite-derived insights. In so doing, it leverages larger sample sizes drawn from 25 rather than 6 years of cases, a modern atmospheric reanalysis dataset at finer resolution that better depicts cyclone structure without using a fictitious vortex, and advances in understanding since H06. Furthermore, this study also presents the first composite analysis of TCs that acquire an extratropical warm-seclusion

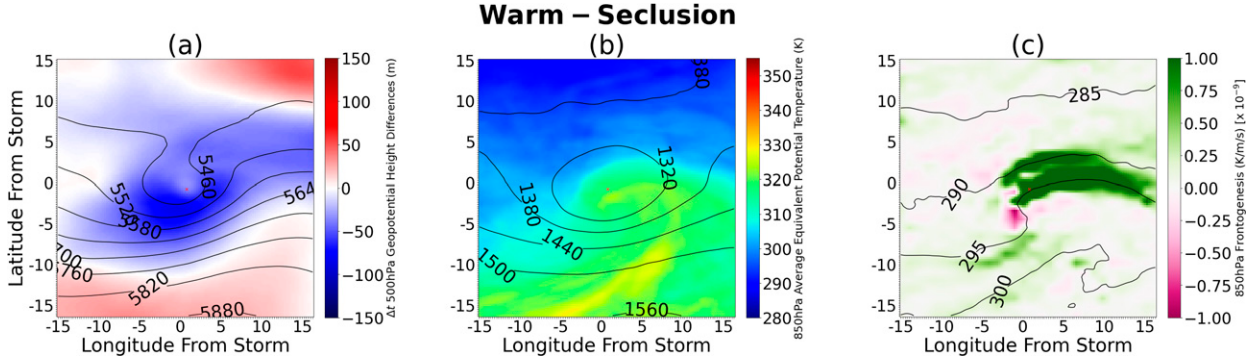


FIG. 13. (a) Composite-mean 500-hPa geopotential height (black contours every 60 m) and composite-mean 500-hPa geopotential height difference (defined as time of warm-seclusion structure acquisition minus CPS-determined  $T_E$ ; shaded per the color bar; m), (b) composite-mean 850-hPa geopotential height (black contours every 60 m) and 850-hPa equivalent potential temperature (shaded per the color bar; K), and (c) 1° smoothed composite-mean 850-hPa two-dimensional kinematic frontogenesis (shaded per the color bar;  $\times 10^{-9}$  K m $^{-1}$  s $^{-1}$ ) for the warm-seclusion composite at the time following  $T_E$  at which each TC acquired a warm-seclusion structure.

structure immediately upon transforming into an extratropical cyclone, here termed instant warm-seclusion cyclones.

Altogether, the results support H06's transformation-stage duration analysis, provides expanded insights into H06's post-transformation intensity-change results, and provides new insights into the large-scale environments supporting post-transformation warm-seclusion structural development. Rapidly and slowly transforming TCs are distinguished by the duration at which the transforming cyclone remains in an environment characterized by warm SSTs after encountering strong baroclinicity (Hart and Evans 2001; H06), with slowly transforming TCs remaining in a region of warmer SSTs throughout the transformation process. Post-transformation strengthening and weakening cyclones are distinguished by the extent to which the transforming cyclone phases with the upstream trough following  $T_E$ , with post-transformation strengthening cyclones better phasing with the upstream trough than do post-transformation weakening cyclones (Klein et al. 2002; Ritchie and Elsberry 2003, 2007). As in H06, the upstream trough acquires a negative tilt in the post-transformation strengthening composite, but this appears to be an outcome rather than harbinger of phasing given that the negative tilt does not develop until proper phasing is achieved. Finally, post-transformation cold-core and warm-seclusion cyclones are distinguished by their downstream synoptic-scale environments, with post-transformation warm-seclusion cyclones moving into a region of strongly confluent flow that facilitates strong lower-tropospheric frontogenesis along their warm and bent-back fronts, strong lower-tropospheric frontolysis along their cold fronts, and their seclusion within relatively warm, moist lower-tropospheric air (Schultz et al. 1998; Schultz and Zhang 2007). Unlike H06, the narrowing of the upstream trough does not appear to be essential for post-transformation warm-seclusion structural development, though this warrants further investigation.

This study also introduces a new ET classification for the North Atlantic basin, here termed instant warm-seclusion given that the cyclones in question acquire a warm-seclusion structure immediately upon (rather than following, as in

Evans and Hart 2003) extratropical transformation. Instant warm-seclusion cyclones bear many similarities to the western North Pacific basin "seclusion–occlusion" cyclones studied by Kitabatake (2008), including their relative frequencies (about one-third of all ET events), propagation speeds (significantly slower than other transforming cyclones), post-transformation intensities (significantly stronger than other transforming cyclones), and post-transformation cyclone structures. Instant warm-seclusion cyclones are characterized by a negatively tilted upstream trough that undergoes cyclonic Rossby wave breaking as the transformation stage ends (Figs. 11c,f,i). Although this synoptic environment significantly differs from that of post-transformation warm-seclusion cyclones (Figs. 11b,c,e,f,h,i), it results in a similar pattern of lower-tropospheric frontogenesis, with strong frontogenesis along the cyclones' bent-back front (Figs. 13c,f,i) and strong frontolysis near the transforming cyclone (Figs. 13c,f,i). Cyclonic Rossby wave breaking may be facilitated by a relatively weak upper-tropospheric jet (Figs. 14c,f,i; Polvani et al. 1989; Polvani and Plumb 1992; Swanson et al. 1997). Note, however, that cyclonic Rossby wave breaking is not exclusively associated with instant warm-seclusion development; while two of the five North Atlantic TCs identified by Jones et al. (2003) to be associated with cyclonic Rossby wave breaking during ET are identified herein as instant warm-seclusion cyclones (Lili 1996 and Gabrielle 2001), the other three are identified as post-transformation warm-seclusion cyclones.

Transforming cyclones' role in facilitating cyclonic Rossby wave breaking during and after the transformation stage, whether it occurs with instant warm-seclusion cyclones or other transforming cyclones, is unclear. For instance, although there is appreciable upper-tropospheric negative potential-vorticity advection by the instant warm-seclusion cyclones' divergent outflow to the northwest (Figs. 14c,f,i), where it could facilitate the upstream trough acquiring a negative tilt and cyclonically breaking (such as with Sandy 2012; Galaneau et al. 2013), this is also true of the post-transformation warm-seclusion and (to lesser extent) cold-core composites (Figs. 14a,b,d,e,g,h) and does not appear to be a distinguishing

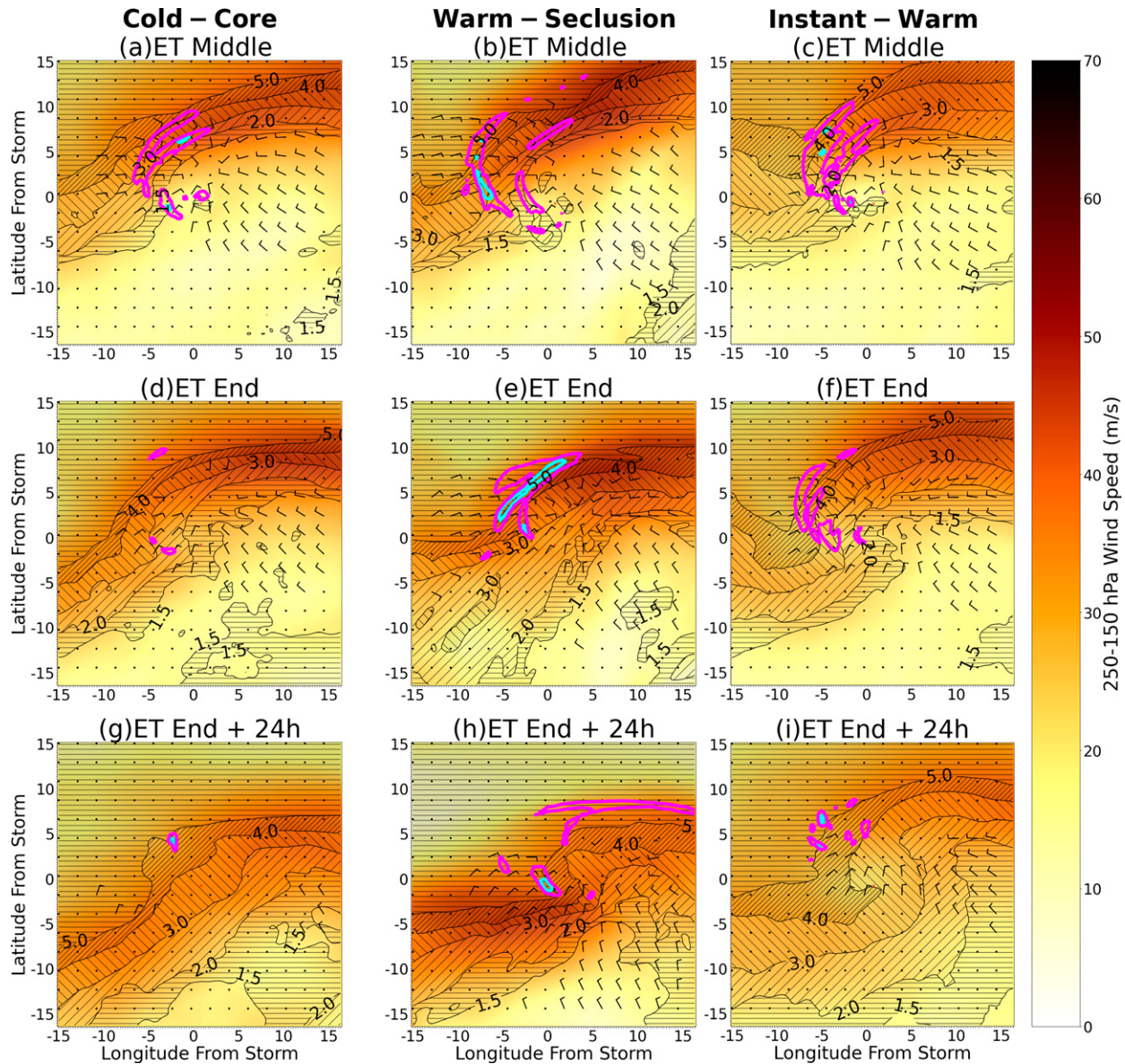


FIG. 14. Composite-mean 250–150-hPa layer-mean PV (contours and hatching at 1.5, 2, 3, 4, and 5 PVU), 250–150-hPa layer-mean horizontal wind speed (shaded per the color bar;  $\text{m s}^{-1}$ ), 250–150-hPa layer-mean irrotational wind (black barbs at  $5 \text{ m s}^{-1}$ ), and 250–150-hPa layer-mean negative PV advection by the irrotational wind (pink and light-blue contours at  $-0.5 \times 10^{-4}$  and  $-1.0 \times 10^{-4}$  PVU  $\text{s}^{-1}$ , respectively) for the post-transformation (left) cold-core; (center) warm-seclusion; and (right) instant warm-seclusion composites at (a)–(c)  $T_{\text{MID}}$ ; (d)–(f)  $T_E$ ; and (g)–(i)  $T_E + 24 \text{ h}$ .

characteristic of instant warm-seclusion events. Furthermore, prior case studies of cyclonic Rossby wave breaking events accompanying ET—Earl (1998, a post-transformation warm-seclusion; McTaggart-Cowan et al. 2001, 2004) and western North Pacific TC Bart (1999; Klein et al. 2002)—imply a minimal role of the transforming TC relative to those of the upstream trough and upper-tropospheric jet in facilitating cyclonic Rossby wave breaking. However, further investigation over a larger sample of events using numerical simulations and PV inversion techniques (e.g., McTaggart-Cowan

et al. 2001, 2003) is needed to better quantify the transforming TCs' roles in facilitating cyclonic Rossby wave breaking during ET.

Unlike post-transformation warm seclusions, instant warm-seclusion cyclones persist in the CPS's asymmetric, shallow warm-core quadrant following transformation (Fig. 2b). As a result, the ET classification criterion that identifies the CPS-derived  $T_E$  as the time that the transforming TC loses its lower-tropospheric warm-core structure (Evans and Hart 2003) limits the CPS's ability to identify instant warm-seclusion events

reliably and objectively. This negatively impacts operational cyclone structure assessments because all operational forecast agencies with TC forecasting responsibilities use the CPS to help diagnose ET (Fogarty 2010; Evans et al. 2017). Consequently, further research is warranted to extend the CPS so it can reliably and objectively identify instant warm-seclusion structure acquisition. In addition, the large differences between the operationally determined and ERA5-based CPS-derived  $T_E$  for instant warm-seclusion cyclones (Fig. 1) suggest that these limitations may also impact transformation timing, duration, and location information in existing CPS-based ET climatologies (e.g., Kitabatake 2011; Wood and Ritchie 2014; Bieli et al. 2019a,b), should the older, coarser reanalysis data used within these studies be able to reliably depict instant warm-seclusion structures. Further research leveraging modern reanalysis datasets is warranted to quantify these impacts and, more generally, develop a global climatology of instant warm-seclusion cyclones.

**Acknowledgments.** The first author was supported during this research by two UW–Milwaukee Support for Undergraduate Research Fellowships. Funding support for this publication was provided by the University of Chicago’s Department of Geophysical Sciences. We acknowledge fruitful conversations about this research with Ben Schenkel and Kimberly Wood, as well as detailed feedback from Editor Ron McTaggart-Cowan and two anonymous reviewers. We thank Kevin Prince for his assistance with bootstrap statistical significance calculations.

**Data availability statement.** ERA5 reanalysis data are available from the NCAR Research Data Archive (<https://doi.org/10.5065/BH6N-5N20>; European Centre for Medium-Range Weather Forecasts 2019). CPS codes are available from Robert Hart at Florida State University (<http://moe.met.fsu.edu/~rhart/phasescripts/>). NHC best track information is available at <https://www.nhc.noaa.gov/data/>. The satellite imagery included with Fig. 1 is available from the Global ISCCP B1 Browse System at <https://www.ncdc.noaa.gov/gibbs/year> (Knapp et al. 2011). NOAA Optimum Interpolation High Resolution SST V2 data are available from the NOAA/OAR/ESRL Physical Sciences Laboratory at <https://psl.noaa.gov/data/gridded/data.noaa.oisst.v2.highres.html>.

## REFERENCES

- Agustí-Panareda, A., S. L. Gray, G. C. Craig, and C. Thorncroft, 2005: The extratropical transition of Tropical Cyclone Lili (1996) and its crucial contribution to a moderate extratropical development. *Mon. Wea. Rev.*, **133**, 1562–1573, <https://doi.org/10.1175/MWR2935.1>.
- Archambault, H. M., L. F. Bosart, D. Keyser, and J. M. Cordeira, 2013: A climatological analysis of the extratropical flow response to recurring western North Pacific tropical cyclones. *Mon. Wea. Rev.*, **141**, 2325–2346, <https://doi.org/10.1175/MWR-D-12-00257.1>.
- , D. Keyser, L. F. Bosart, C. A. Davis, and J. M. Cordeira, 2015: A composite perspective of the extratropical flow response to recurring western North Pacific tropical cyclones. *Mon. Wea. Rev.*, **143**, 1122–1141, <https://doi.org/10.1175/MWR-D-14-00270.1>.
- Benjamini, Y., and Y. Hochberg, 1995: Controlling the false discovery rate: A practical and powerful approach to multiple testing. *J. Roy. Stat. Soc.*, **57B**, 289–300, <https://doi.org/10.1111/j.2517-6161.1995.tb02031.x>.
- Bian, G.-F., G.-Z. Nie, and X. Qiu, 2021: How well is outer tropical cyclone size represented in the ERA5 reanalysis dataset? *Atmos. Res.*, **249**, 105339, <https://doi.org/10.1016/j.atmosres.2020.105339>.
- Bieli, M., S. J. Camargo, A. H. Sobel, J. L. Evans, and T. Hall, 2019a: A global climatology of extratropical transition. Part I: Characteristics across basins. *J. Climate*, **32**, 3557–3582, <https://doi.org/10.1175/JCLI-D-17-0518.1>.
- , —, —, —, and —, 2019b: A global climatology of extratropical transition. Part II: Statistical performance of the cyclone phase space. *J. Climate*, **32**, 3583–3597, <https://doi.org/10.1175/JCLI-D-18-0052.1>.
- Bister, M., and K. A. Emanuel, 2002: Low frequency variability of tropical cyclone potential intensity. Part I: Interannual to interdecadal variability. *J. Geophys. Res.*, **107**, 4801, <https://doi.org/10.1029/2001JD000776>.
- Bluestein, H., 1993: *Synoptic-Dynamic Meteorology in Midlatitudes. Vol. II: Observations and Theory of Weather Systems*. Oxford University Press, 594 pp.
- Bosart, L. F., C. S. Velden, W. E. Bracken, J. Molinari, and P. G. Black, 2000: Environmental influences on the rapid intensification of Hurricane Opal (1995) over the Gulf of Mexico. *Mon. Wea. Rev.*, **128**, 322–352, [https://doi.org/10.1175/1520-0493\(2000\)128<0322:EIOTRI>2.0.CO;2](https://doi.org/10.1175/1520-0493(2000)128<0322:EIOTRI>2.0.CO;2).
- Bracken, W. E., and L. F. Bosart, 1998: Multiple development aspects of Hurricane Opal (1995). Preprints, *Symp. on Tropical Cyclone Intensity Change*, Phoenix, AZ, Amer. Meteor. Soc., 99–104.
- Browning, K. A., G. Vaughan, and P. Panagi, 1998: Analysis of an ex-tropical cyclone after its re-intensification as a warm-core extratropical cyclone. *Quart. J. Roy. Meteor. Soc.*, **124**, 2329–2356, <https://doi.org/10.1002/qj.49712455108>.
- Dawson, A., 2016: Windspharm: A high-level library for global wind field computations using spherical harmonics. *J. Open Res. Software*, **4**, e31, <https://doi.org/10.5334/jors.129>.
- Dee, D. P., and Coauthors, 2011: The ERA-Interim reanalysis: Configuration and performance of the data assimilation system. *Quart. J. Roy. Meteor. Soc.*, **137**, 553–597, <https://doi.org/10.1002/qj.828>.
- Dullaart, J. C. M., S. Muis, N. Bloemendaal, and J. C. J. H. Aerts, 2019: Advancing global storm surge modelling using the new ERA5 climate reanalysis. *Climate Dyn.*, **54**, 1007–1021, <https://doi.org/10.1007/s00382-019-05044-0>.
- Efron, B., 1979: Bootstrap methods: Another look at the jackknife. *Ann. Stat.*, **7**, 1–26, <https://doi.org/10.1214/aos/1176344552>.
- European Centre for Medium-Range Weather Forecasts, 2019: ERA5 Reanalysis (0.25 Degree Latitude-Longitude Grid). Research Data Archive at the National Center for Atmospheric Research, Computational and Information Systems Laboratory, accessed 11 October 2022, <https://doi.org/10.5065/BH6N-5N20>.
- Evans, C., and Coauthors, 2017: The extratropical transition of tropical cyclones. Part I: Cyclone evolution and direct impacts. *Mon. Wea. Rev.*, **145**, 4317–4344, <https://doi.org/10.1175/MWR-D-17-0027.1>.

- Evans, J. L., and R. E. Hart, 2003: Objective indicators of the life cycle evolution of extratropical transition for Atlantic tropical cyclones. *Mon. Wea. Rev.*, **131**, 909–925, [https://doi.org/10.1175/1520-0493\(2003\)131<0909:OIOTLC>2.0.CO;2](https://doi.org/10.1175/1520-0493(2003)131<0909:OIOTLC>2.0.CO;2).
- , and B. E. Prater-Mayes, 2004: Factors affecting the post-transition intensification of Hurricane Irene (1999). *Mon. Wea. Rev.*, **132**, 1355–1368, [https://doi.org/10.1175/1520-0493\(2004\)132<1355:FATPIO>2.0.CO;2](https://doi.org/10.1175/1520-0493(2004)132<1355:FATPIO>2.0.CO;2).
- Galarneau, T. J., C. A. Davis, and M. A. Shapiro, 2013: Intensification of Hurricane Sandy (2012) through extratropical warm core seclusion. *Mon. Wea. Rev.*, **141**, 4296–4321, <https://doi.org/10.1175/MWR-D-13-00181.1>.
- Gilford, D. M., 2021: pyPI (v1.3): Tropical cyclone potential intensity calculations in Python. *Geosci. Model Dev.*, **14**, 2351–2369, <https://doi.org/10.5194/gmd-14-2351-2021>.
- Goerss, J. S., and R. A. Jeffries, 1994: Assimilation of synthetic tropical cyclone observations into the Navy Operational Global Atmospheric Prediction System. *Wea. Forecasting*, **9**, 557–576, [https://doi.org/10.1175/1520-0434\(1994\)009<0557:AOSTCO>2.0.CO;2](https://doi.org/10.1175/1520-0434(1994)009<0557:AOSTCO>2.0.CO;2).
- Harr, P. A., and R. L. Elsberry, 2000: Extratropical transition of tropical cyclones over the western North Pacific. Part I: Evolution of structural characteristics during the transition process. *Mon. Wea. Rev.*, **128**, 2613–2633, [https://doi.org/10.1175/1520-0493\(2000\)128<2613:ETOTCO>2.0.CO;2](https://doi.org/10.1175/1520-0493(2000)128<2613:ETOTCO>2.0.CO;2).
- , —, and T. F. Hogan, 2000: Extratropical transition of tropical cyclones over the western North Pacific. Part II: The impact of midlatitude circulation characteristics. *Mon. Wea. Rev.*, **128**, 2634–2653, [https://doi.org/10.1175/1520-0493\(2000\)128<2634:ETOTCO>2.0.CO;2](https://doi.org/10.1175/1520-0493(2000)128<2634:ETOTCO>2.0.CO;2).
- Hart, R. E., 2003: A cyclone phase space derived from thermal wind and thermal asymmetry. *Mon. Wea. Rev.*, **131**, 585–616, [https://doi.org/10.1175/1520-0493\(2003\)131<0585:ACPSDF>2.0.CO;2](https://doi.org/10.1175/1520-0493(2003)131<0585:ACPSDF>2.0.CO;2).
- , and J. L. Evans, 2001: A climatology of the extratropical transition of Atlantic tropical cyclones. *J. Climate*, **14**, 546–564, [https://doi.org/10.1175/1520-0442\(2001\)014<0546:ACOTET>2.0.CO;2](https://doi.org/10.1175/1520-0442(2001)014<0546:ACOTET>2.0.CO;2).
- , —, and C. Evans, 2006: Synoptic composites of the extratropical transition life cycle of North Atlantic tropical cyclones: Factors determining post-transition evolution. *Mon. Wea. Rev.*, **134**, 553–578, <https://doi.org/10.1175/MWR3082.1>.
- Hersbach, H., 2019: ECMWF's ERA5 reanalysis extends back to 1979. ECMWF Newsletter, No. 158, ECMWF, Reading, United Kingdom, 1, <https://www.ecmwf.int/en/newsletter/158/news/ecmwf-ers5-reanalysis-extends-back-1979>.
- , and Coauthors, 2020: The ERA5 global reanalysis. *Quart. J. Roy. Meteor. Soc.*, **146**, 1999–2049, <https://doi.org/10.1002/qj.3803>.
- Hines, K. M., and C. R. Mechoso, 1993: Influence of surface drag on the evolution of fronts. *Mon. Wea. Rev.*, **121**, 1152–1176, [https://doi.org/10.1175/1520-0493\(1993\)121<1152:IOSDOT>2.0.CO;2](https://doi.org/10.1175/1520-0493(1993)121<1152:IOSDOT>2.0.CO;2).
- Hogan, T. F., and T. E. Rosmond, 1991: The description of the Navy Operational Global Atmospheric Prediction System's spectral forecast model. *Mon. Wea. Rev.*, **119**, 1786–1815, [https://doi.org/10.1175/1520-0493\(1991\)119<1786:TDOTNO>2.0.CO;2](https://doi.org/10.1175/1520-0493(1991)119<1786:TDOTNO>2.0.CO;2).
- Hoskins, B. J., and P. J. Valdes, 1990: On the existence of storm-tracks. *J. Atmos. Sci.*, **47**, 1854–1864, [https://doi.org/10.1175/1520-0469\(1990\)047<1854:OTEOST>2.0.CO;2](https://doi.org/10.1175/1520-0469(1990)047<1854:OTEOST>2.0.CO;2).
- Jones, S. C., and Coauthors, 2003: The extratropical transition of tropical cyclones: Forecast challenges, current understanding, and future directions. *Wea. Forecasting*, **18**, 1052–1092, [https://doi.org/10.1175/1520-0434\(2003\)018<1052:TETOTC>2.0.CO;2](https://doi.org/10.1175/1520-0434(2003)018<1052:TETOTC>2.0.CO;2).
- Keller, J. H., and Coauthors, 2019: The extratropical transition of tropical cyclones. Part II: Interaction with the midlatitude flow, downstream impacts, and implications for predictability. *Mon. Wea. Rev.*, **147**, 1077–1106, <https://doi.org/10.1175/MWR-D-17-0329.1>.
- Kitabatake, N., 2008: Extratropical transition of tropical cyclones in the western North Pacific: Their frontal evolution. *Mon. Wea. Rev.*, **136**, 2066–2090, <https://doi.org/10.1175/2007MWR1958.1>.
- , 2011: Climatology of extratropical transition of tropical cyclones in the western North Pacific defined by using cyclone phase space. *J. Meteor. Soc. Japan*, **89**, 309–325, <https://doi.org/10.2151/jmsj.2011-402>.
- Klein, P. M., P. A. Harr, and R. Elsberry, 2000: Extratropical transition of western North Pacific tropical cyclones: An overview and conceptual model of the transformation stage. *Wea. Forecasting*, **15**, 373–395, [https://doi.org/10.1175/1520-0434\(2000\)015<0373:ETOWNP>2.0.CO;2](https://doi.org/10.1175/1520-0434(2000)015<0373:ETOWNP>2.0.CO;2).
- , —, and R. L. Elsberry, 2002: Extratropical transition of western North Pacific tropical cyclones: Midlatitude and tropical cyclone contributions to reintensification. *Mon. Wea. Rev.*, **130**, 2240–2259, [https://doi.org/10.1175/1520-0493\(2002\)130<2240:ETOWNP>2.0.CO;2](https://doi.org/10.1175/1520-0493(2002)130<2240:ETOWNP>2.0.CO;2).
- Knapp, K. R., and Coauthors, 2011: Globally gridded satellite (GridSat) observations for climate studies. *Bull. Amer. Meteor. Soc.*, **92**, 893–907, <https://doi.org/10.1175/2011BAMS3039.1>.
- Kuo, Y., R. J. Reed, and S. Low-Nam, 1992: Thermal structure and airflow in a model simulation of an occluded marine cyclone. *Mon. Wea. Rev.*, **120**, 2280–2297, [https://doi.org/10.1175/1520-0493\(1992\)120<2280:TSAAIA>2.0.CO;2](https://doi.org/10.1175/1520-0493(1992)120<2280:TSAAIA>2.0.CO;2).
- Landsea, C. W., and J. L. Franklin, 2013: Atlantic hurricane database uncertainty and presentation of a new database format. *Mon. Wea. Rev.*, **141**, 3576–3592, <https://doi.org/10.1175/MWR-D-12-00254.1>.
- Malakar, P., A. P. Kesarkar, J. N. Bhate, V. Singh, and A. Deshamukhya, 2020: Comparison of reanalysis datasets to comprehend the evolution of tropical cyclones over North Indian Ocean. *Earth Space Sci.*, **7**, e2019EA000978, <https://doi.org/10.1029/2019EA000978>.
- Mass, C. F., and D. M. Schultz, 1993: The structure and evolution of a simulated midlatitude cyclone over land. *Mon. Wea. Rev.*, **121**, 889–917, [https://doi.org/10.1175/1520-0493\(1993\)121<0889:TSAEOA>2.0.CO;2](https://doi.org/10.1175/1520-0493(1993)121<0889:TSAEOA>2.0.CO;2).
- Masson, A., 2014: The extratropical transition of Hurricane Igor and the impacts on Newfoundland. *Nat. Hazards*, **72**, 617–632, <https://doi.org/10.1007/s11069-013-1027-x>.
- May, R. M., and Coauthors, 2022: MetPy: A Python package for meteorological data. Unidata, accessed 11 October 2022, <https://doi.org/10.5065/D6WW7G29>.
- McTaggart-Cowan, R., J. R. Gyakum, and M. K. Yau, 2001: Sensitivity testing of extratropical transitions using potential vorticity inversions to modify initial conditions: Hurricane Earl case study. *Mon. Wea. Rev.*, **129**, 1617–1636, [https://doi.org/10.1175/1520-0493\(2001\)129<1617:STOETU>2.0.CO;2](https://doi.org/10.1175/1520-0493(2001)129<1617:STOETU>2.0.CO;2).
- , —, and —, 2003: The influence of the downstream state on extratropical transition: Hurricane Earl (1998) case study. *Mon. Wea. Rev.*, **131**, 1910–1929, <https://doi.org/10.1175//2589.1>.

- , —, and —, 2004: The impact of tropical remnants on extratropical cyclogenesis: Case study of Hurricanes Danielle and Earl (1998). *Mon. Wea. Rev.*, **132**, 1933–1951, [https://doi.org/10.1175/1520-0493\(2004\)132<1933:TIOTRO>2.0.CO;2](https://doi.org/10.1175/1520-0493(2004)132<1933:TIOTRO>2.0.CO;2).
- Molinari, J., S. Skubis, and D. Vollaro, 1995: External influences on hurricane intensity. Part III: Potential vorticity structure. *J. Atmos. Sci.*, **52**, 3593–3606, [https://doi.org/10.1175/1520-0469\(1995\)052<3593:EIOHIP>2.0.CO;2](https://doi.org/10.1175/1520-0469(1995)052<3593:EIOHIP>2.0.CO;2).
- , —, —, F. Alsheimer, and H. E. Willoughby, 1998: Potential vorticity analysis of tropical cyclone intensification. *J. Atmos. Sci.*, **55**, 2632–2644, [https://doi.org/10.1175/1520-0469\(1998\)055<2632:PVAOTC>2.0.CO;2](https://doi.org/10.1175/1520-0469(1998)055<2632:PVAOTC>2.0.CO;2).
- Neu, U., and Coauthors, 2013: IMILAST: A community effort to intercompare extratropical cyclone detection and tracking algorithms. *Bull. Amer. Meteor. Soc.*, **94**, 529–547, <https://doi.org/10.1175/BAMS-D-11-00154.1>.
- Pantillon, F., J.-P. Chaboureau, C. Lac, and P. Mascart, 2013: On the role of a Rossby wave train during the extratropical transition of Hurricane Helene (2006). *Quart. J. Roy. Meteor. Soc.*, **139**, 370–386, <https://doi.org/10.1002/qj.1974>.
- Petterssen, S., 1955: A general survey of factors influencing development at sea level. *J. Meteor.*, **12**, 36–42, [https://doi.org/10.1175/1520-0469\(1955\)012<0036:AGSOFI>2.0.CO;2](https://doi.org/10.1175/1520-0469(1955)012<0036:AGSOFI>2.0.CO;2).
- Polvani, L. M., and R. A. Plumb, 1992: Rossby wave breaking, filamentation, and secondary vortex formation: The dynamics of a perturbed vortex. *J. Atmos. Sci.*, **49**, 462–476, [https://doi.org/10.1175/1520-0469\(1992\)049<0462:RWBMFA>2.0.CO;2](https://doi.org/10.1175/1520-0469(1992)049<0462:RWBMFA>2.0.CO;2).
- , G. R. Flierl, and N. J. Zabusky, 1989: Filamentation of unstable vortex structures via separatrix crossing: A quantitative estimate of onset time. *Phys. Fluids A Fluid Dyn.*, **1**, 181–184, <https://doi.org/10.1063/1.857485>.
- Rantanen, M., J. Räisänen, V. A. Sinclair, J. Lento, and H. Järvinen, 2020: The extratropical transition of Hurricane Ophelia (2017) as diagnosed with a generalized omega equation and vorticity equation. *Tellus*, **72A**, 1721215, <https://doi.org/10.1080/16000870.2020.1721215>.
- Reynolds, R. W., T. M. Smith, C. Liu, D. B. Chelton, K. S. Casey, and M. G. Schlax, 2007: Daily high-resolution-blended analyses for sea surface temperature. *J. Climate*, **20**, 5473–5496, <https://doi.org/10.1175/2007JCLI1824.1>.
- Ritchie, E. A., and R. L. Elsberry, 2003: Simulations of the extratropical transition of tropical cyclones: Contributions by the midlatitude upper-level trough to reintensification. *Mon. Wea. Rev.*, **131**, 2112–2128, [https://doi.org/10.1175/1520-0493\(2003\)131<2112:SOTETO>2.0.CO;2](https://doi.org/10.1175/1520-0493(2003)131<2112:SOTETO>2.0.CO;2).
- , and —, 2007: Simulations of the extratropical transition of tropical cyclones: Phasing between the upper-level trough and tropical cyclones. *Mon. Wea. Rev.*, **135**, 862–876, <https://doi.org/10.1175/MWR3303.1>.
- Sainsbury, E. M., R. K. H. Schiemann, K. I. Hodges, L. C. Shaffery, A. J. Baker, and K. T. Bhatia, 2020: How important are post-tropical cyclones for European windstorm risk? *Geophys. Res. Lett.*, **47**, e2020GL089853, <https://doi.org/10.1029/2020GL089853>.
- Schultz, D. M., and F. Zhang, 2007: Baroclinic development within zonally-varying flows. *Quart. J. Roy. Meteor. Soc.*, **133**, 1101–1112, <https://doi.org/10.1002/qj.87>.
- , D. Keyser, and L. F. Bosart, 1998: The effect of large-scale flow on low-level frontal structure and evolution in midlatitude cyclones. *Mon. Wea. Rev.*, **126**, 1767–1791, [https://doi.org/10.1175/1520-0493\(1998\)126<1767:TEOLSF>2.0.CO;2](https://doi.org/10.1175/1520-0493(1998)126<1767:TEOLSF>2.0.CO;2).
- , and Coauthors, 2019: Extratropical cyclones: A century of research on meteorology's centerpiece. *A Century of Progress in Atmospheric and Related Sciences: Celebrating the American Meteorological Society Centennial*, Meteor. Monogr., No. 59, Amer. Meteor. Soc., <https://doi.org/10.1175/AMSMONOGRAPHSD-18-0015.1>.
- Shapiro, L. J., and D. Keyser, 1990: Fronts, jet streams, and the tropopause. *Extratropical Cyclones: The Erik Palmen Memorial Volume*, C. W. Newton and E. O. Holopainen, Eds., Amer. Meteor. Soc., 167–191.
- Studholme, J., K. I. Hodges, and C. M. Brierly, 2015: Objective determination of the extratropical transition of tropical cyclones in the Northern Hemisphere. *Tellus*, **67A**, 24474, <https://doi.org/10.3402/tellusa.v67.24474>.
- Sun, Y., Z. Zhong, and Y. Wang, 2012: Kinetic energy budget of Typhoon Yagi (2006) during its extratropical transition. *Meteor. Atmos. Phys.*, **118**, 65–78, <https://doi.org/10.1007/s00703-012-0200-1>.
- Sutcliffe, R. C., and A. G. Forsdyke, 1950: The theory and use of upper air thickness patterns in forecasting. *Quart. J. Roy. Meteor. Soc.*, **76**, 189–217, <https://doi.org/10.1002/qj.49707632809>.
- Swanson, K. L., P. J. Kushner, and I. M. Held, 1997: Dynamics of barotropic storm tracks. *J. Atmos. Sci.*, **54**, 791–810, [https://doi.org/10.1175/1520-0469\(1997\)054<0791:DOBST>2.0.CO;2](https://doi.org/10.1175/1520-0469(1997)054<0791:DOBST>2.0.CO;2).
- Thorncroft, C. D., and S. C. Jones, 2000: The extratropical transitions of Hurricanes Felix and Iris in 1995. *Mon. Wea. Rev.*, **128**, 947–972, [https://doi.org/10.1175/1520-0493\(2000\)128<0947:TETOHF>2.0.CO;2](https://doi.org/10.1175/1520-0493(2000)128<0947:TETOHF>2.0.CO;2).
- , B. J. Hoskins, and M. E. McIntyre, 1993: Two paradigms of baroclinic-wave life-cycle behaviour. *Quart. J. Roy. Meteor. Soc.*, **119**, 17–55, <https://doi.org/10.1002/qj.49711950903>.
- Wilks, D. S., 2006: *Statistical Methods in the Atmospheric Sciences*. 2nd ed. International Geophysics Series, Vol. 100, Academic Press, 648 pp.
- , 2016: “The stippling shows statistically significant grid points”: How research results are routinely overstated and overinterpreted, and what to do about it. *Bull. Amer. Meteor. Soc.*, **97**, 2263–2273, <https://doi.org/10.1175/BAMS-D-15-00267.1>.
- Wood, K. M., and E. A. Ritchie, 2014: A 40-year climatology of extratropical transition in the eastern North Pacific. *J. Climate*, **27**, 5999–6015, <https://doi.org/10.1175/JCLI-D-13-00645.1>.